



Milestone Report

Device-scale CFD study for mass transfer coefficient and effective mass transfer area in packed column

Work Performed Under
Activity Number 0004000.6.600.007.002 ARRA

Prepared by
Pacific Northwest National Laboratory
Richland, Washington 99352
PNNL – 28161

Prepared for the
U.S. Department of Energy
National Energy Technology Laboratory

October 2018



Revision Log

Revision	Date	Revised By:	Description
0.1	10/03/18	Jie Bao and Rajesh Singh	Original draft
0.2	10/07/18	Rajesh Singh	First consolidating draft
0.3	10/12/18	Rajesh Singh and Zhijie Xu	1 st revision with formatting
0.4	10/16/18	Rajesh Singh	2 nd revision with formatting and proof reading
0.5	10/24/18	Rajesh Singh and Zhijie Xu	Final Proof Reading
0.6	10/26/2018	Charles Freeman and Rajesh Singh	Proof Reading

Disclaimer

This report was prepared as an account of work sponsored by an agency of the United States Government. Neither the United States Government nor any agency thereof, nor any of their employees, makes any warranty, express or implied, or assumes any legal liability or responsibility for the accuracy, completeness, or usefulness of any information, apparatus, product, or process disclosed, or represents that its use would not infringe privately owned rights. Reference herein to any specific commercial product, process, or service by trade name, trademark, manufacturer, or otherwise does not necessarily constitute or imply its endorsement, recommendation, or favoring by the United States Government or any agency thereof. The views and opinions of authors expressed herein do not necessarily state or reflect those of the United States Government or any agency thereof.

Acknowledgment of Funding

This project was funded under the Carbon Capture Simulation for Industry Impact (CCSI²) under the following FWPs and contracts:

PNNL – 68494

Contents

Nomenclature.....	vi
Acronyms.....	vii
Executive Summary.....	viii
1.0 Background.....	1
2.0 Methodology.....	2
2.1 Mathematical Formulations.....	2
2.2 Species Transport Equation.....	3
2.3 Reaction Chemistry for Absorption of CO ₂ in Aqueous NaOH Solution.....	3
2.4 Reaction Kinetics for Absorption of CO ₂ in Aqueous MEA Solvent.....	4
2.5 Numerical Scheme.....	5
3.0 Direct Effect of Solvent Viscosity on the Physical Mass Transfer in a Packed Column.....	6
3.1 Introduction.....	6
3.2 Mathematical Formulation of the Physical Mass Transfer.....	8
3.3 Problem Setup.....	15
3.4 Results and Discussion.....	17
3.4.1 Film Thickness.....	17
3.4.2 Mass Transfer Coefficient.....	18
4.0 Multiphase Flow Investigations in the Structured Packings.....	22
4.1 Introduction.....	22
4.2 Problem Setup.....	23
4.3 Results and Discussions.....	26
4.3.1 Comparison with Experiments at Different Liquid Loads.....	27
4.3.2 Effect of Solvent Properties.....	30
4.3.3 Effects of Contact Angle.....	30
5.0 Multiphase Flow Simulations in Random Ring Packings.....	33
5.1 Introduction.....	33
5.2 Simulation Geometry and Boundary Conditions.....	33
5.3 Results.....	35
6.0 Conclusion.....	40
7.0 References.....	42

List of Figures

Figure 1.	Schematic description of a wavy film falling over a vertical plate, where u and v are vertical and horizontal velocity, respectively. The falling film with an average thickness δ_0 can be described by a rolling wave with an amplitude A , a wavelength λ , and a wave speed u_w .	8
Figure 2.	Variation of normalized wave amplitude (A/λ) with ratio of wave velocity components (V_y/V_x) at different Reynolds numbers. It shows the linear scaling ($A/\lambda \sim V_y/V_x$) and independence of Reynolds number.	11
Figure 3.	(a) Variation of the normalized wave amplitude (A/λ) with Reynolds number at $Ka=2850$. (b) Variation of (A/λ) with Ka at two Reynolds numbers shows that normalized amplitude decreases with increased Kapitza number.	12
Figure 4.	Variation of normalized wave amplitude with Reynolds and Kapitza numbers shows the scaling $A/\lambda \sim Re^{0.78}Ka^{-0.47}$. The exponents of the fitting for Re and Ka reasonably match the previous studies by Shkadov [53].	12
Figure 5.	Schematic of flow domain showing the inlet and outlet positions for both phases: (a) wetted wall column and (b) zigzag column as 2D representative of structured packings. The inlet and outlet of both phases have 1 mm width. (c) The dark region at the left in the exploded view of the discretized domain shows very fine mesh to capture the mass transfer phenomenon.	15
Figure 6.	(a) Plot shows variation of the film thickness (δ) with solvent viscosity (μ_L) for the WWC. Predicted value of the film thickness matches well with Nusselt theory [34]. (b) Variation of the normalized film thickness with Kapitza number. Inset of (b) shows the scaling relation of $\delta^* \sim Ka^{1/4}$.	17
Figure 7.	Plot shows variation of the normalized wavelength (λ^*) in a periodic wavy film with Kapitza number (Ka) for WWC and ZZC. Inset shows the wavy film (red color) and method to compute wavelength.	18
Figure 8.	Variation of the mass transfer coefficient (k_L) with solvent viscosity (μ_L) wetted wall column and zigzag column in the case of a smooth and uniform film.	19
Figure 9	Exploded view in the triangular channel shows velocity streamline and concentration distribution in the flow domain. It also illustrates the recirculation zones on the gas side due to triangular geometry.	20
Figure 10.	Variation of the mass transfer coefficient (k_L) with solvent viscosity (μ_L) for smooth and wavy film flow in: (a) wetted wall column and (b) zigzag column. Prefix U: Uniform and O: Oscillatory Inlet.	21
Figure 11.	(a) Comparison of the variation of the mass transfer coefficient with solvent viscosity for analytically derived expression (Eq. 25) and CFD simulations for OWWC. Both reasonably show the same trend of the variation of mass transfer coefficient with viscosity. (b) Variation of the mass transfer coefficient (k_L) with solvent viscosity (ν_L) shows a scaling $k_L \sim \nu_L^{-0.34}$ for OWWC.	21
Figure 12.	(a) An image of a typical structured packing shows the side-by-side arrangement of corrugated sheets. Exploded view explains the selection of current model in the flow simulations (Source: https://www.sulzer.com). (b) The corrugated sheet design used to construct the REU of Mellapak 250.Y structured packing for the CFD simulations.	24
Figure 13.	(a) 3D view of the computational flow domain of REU shows the countercurrent flow direction of gas and solvents. The periodic boundary is specified at the side of the	

	domain. Liquid is introduced along the inner perimeter of the top and gas was fed from the bottom of flow domain. (b) Meshing of the flow domain shows the polyhedral cells used in flow domain and very fine mesh near the sheet where gas-liquid interface is expected to exist (see the exploded view).	25
Figure 14.	Temporal evolution of the CO ₂ flux at the inlet and outlet of the flow domain. The pseudo-steady state was assumed when the CO ₂ flux at the inlet and outlet remains constant.....	28
Figure 15.	(a) Comparison of the CFD-predicted fractional area with experimental predicted area by Tsai et al. [88] at different liquid loads. Typical snapshots for (a) wetted and (c) interfacial area in the REU at $q_L = 49 \text{ m}^3/\text{m}^2\text{h}$	29
Figure 16.	Effect of liquid load on the interfacial area for two solvents. 30MEA shows a slightly higher value of the interfacial area than the corresponding one for NaOH.....	30
Figure 17.	Variation of the normalized effective (A_{Wn}) and interfacial (A_{In}) areas with contact angle (γ) for 40MEA ($K_a=443$) at $q_L = 62 \text{ m}^3/\text{m}^2\text{h}$. Over prediction in the effective (points in the green elliptic boundary) at higher contact angle is a consequence of grid resolutions.	31
Figure 18.	Pseudo-steady shape of the interface in the REU (i.e., both sheets) for 40 MEA at $q_L = 62 \text{ m}^3/\text{m}^2\text{h}$ and different contact angles ($\gamma = 70^\circ$ to $\gamma = 10^\circ$). The transition from film to rivulet flow occurs for a value around $\gamma = 40^\circ$ for this solvent.	32
Figure 19.	Geometry: (a) single pall ring dimensions; (b) random packed pall ring column.	34
Figure 20.	Inlet and outlet boundary conditions used in the flow simulations: (a) top view and (b) side view.	34
Figure 21.	Sketch demonstrating the liquid-gas interface and wetted surface.....	35
Figure 22.	Liquid distribution (blue color) at the central vertical plane of the column at liquid loads (a) 12.2, (b) 48.9, and (c) $73.3 \text{ m}^3/\text{m}^2\text{h}$	37
Figure 23.	Velocity distribution at the central vertical plane of packed column at liquid loads: (a) 12.2, (b) 48.9, and (c) $73.3 \text{ m}^3/\text{m}^2\text{h}$	37
Figure 24.	CO ₂ concentration in the packed column at liquid loads (a) 12.2, (b) 48.9, and (c) $73.3 \text{ m}^3/\text{m}^2\text{h}$	38
Figure 25.	Comparison of the CFD-predicted effective area, gas-liquid interfacial area, wetted area, and effective area computed from the empirical correlation by Song et al. [2].	39
Figure 26.	Zoomed view of a cross section of the random ring packed column. The blue and grey color denote the liquid and gas phase, respectively.	39

List of Tables

Table 1.	Details of the cases in flow simulation.....	16
Table 2.	Design of the corrugated sheet used in Mellapak 250.Y.....	26
Table 3.	Physical properties of solvents used in flow simulations.	26
Table 4.	Liquid and gas fluids properties.	36

Nomenclature

Symbols	
D_G	CO ₂ diffusivity in gas [$m^2 \cdot s^{-1}$]
D_L	CO ₂ diffusivity in liquid [$m^2 \cdot s^{-1}$]
F_c	Particle surface contact force [N]
F_g	Gravity force [N]
I_p	Moment of inertia of particle [$kg \cdot m^2$]
Ka	Kapitza number
M_c	The moment acts on an individual particle due to contact force [$kg \cdot m^2 \cdot s^{-2}$]
S_c	Species source term [$mol \cdot m^{-3} \cdot s^{-1}$]
S_w	Ring wall surface area [m^2]
a_p	Total packed surface area to volume ratio [m^{-1}]
a_e	Effective reaction surface area to volume ratio [m^{-1}]
c_s	MEA concentration [$mol \cdot m^{-3}$]
f_b	Body force [$kg \cdot m^{-2} \cdot s^{-2}$]
f_δ	Surface tension force [$kg \cdot m^{-2} \cdot s^{-2}$]
k'_g	Mass transfer coefficient [$mol \cdot Pa^{-1} \cdot s^{-1} \cdot m^{-2}$]
m_p	Mass of the particle [kg]
u_G	Gas velocity in packed column [$m \cdot s^{-1}$]
u_L	Liquid velocity in packed column [$m \cdot s^{-1}$]
v_p	Velocity of particle [$m \cdot s^{-1}$]
μ_g	Viscosity of gas [$Pa \cdot s$]
μ_l	Viscosity of liquid [$Pa \cdot s$]
ρ_g	Density of gas [$kg \cdot m^{-3}$]
ρ_l	Density of liquid [$kg \cdot m^{-3}$]
ω_p	Angular velocity of particle [s^{-1}]
D	Diffusivity [$m^2 \cdot s^{-1}$]
H	Henry's constant [–]
R	Gas constant [$J \cdot mol^{-1} \cdot K$]
T	Temperature [K]
Z	Height of the packed column [m]
a	The coefficient to control the source term [–]
b	The coefficient to control the source term [–]
c	Molar concentration [$mol \cdot m^{-3}$]
g	Gravitational acceleration [$m \cdot s^{-2}$]
p	Pressure [Pa]
r	Reaction rate [$m^3 \cdot mol^{-1} \cdot s^{-1}$]
v	Velocity [$m \cdot s^{-1}$]
∇	Gradient operator [m^{-1}]
α	Volume fraction of liquid [–]
δ	Surface tension coefficient [$N \cdot m^{-1}$]

η	Coefficient controlled by the type and material of the packed column [–]
κ	Curvature [m^{-1}]
μ	Viscosity [$Pa \cdot s$]
ρ	Density [$kg \cdot m^{-3}$]

Acronyms

AMG	algebraic multigrid method
CCSI ²	Carbon Capture Simulation for Industry Impact
CFD	computational fluid dynamics
CFL	Courant–Friedrichs–Lewy
CO ₂	carbon dioxide
CO ₂ BOL	CO ₂ binding organic liquids
DEM	discrete element method
HPC	high performance computing
HRIC	high-resolution interface capturing
LBE	lattice Boltzmann equation
MEA	monoethanolamine
N ₂ O	nitrous oxide
NaOH	sodium hydroxide
OWWC	oscillatory inlet in wetted wall column
OZZC	oscillatory inlet in zigzag column
PIC	PNNL Institutional Computing
PNNL	Pacific Northwest National Laboratory
REU	representative elementary unit
SIMPLE	Semi-Implicit Method for Pressure-Linked Equations
SPH	smooth particle hydrodynamics
UWWC	uniform film flow in wetted wall column
UZZC	uniform film flow in zigzag column
VOF	volume of fluid method
WWC	wetted wall column
ZZC	zigzag column

Executive Summary

Coal-fired power plants are a large source of anthropogenic carbon dioxide (CO₂) emissions worldwide. Post-combustion carbon capture by chemical absorption can be a promising technology to reduce CO₂ emission from power plants. The absorption is carried out via countercurrent flow in the packed columns. Monoethanolamine (MEA) is a commercial solvent option for post-combustion capture, but requires significant energy to operate. Alternate solvents are being explored as a means of reducing the energy for carbon capture. These include CO₂ binding organic liquids (CO₂BOL), a water-lean solvent currently being developed as a prospective carbon capture solvent at the Pacific Northwest National Laboratory. The purpose of the current work is to demonstrate the efficacy of computational fluid dynamics (CFD) as a useful tool to understand the behavior of CO₂BOLs and other new advanced solvents in the packed column, where hydrodynamics and mass transfer phenomena are unknown. This report demonstrates the validation of multiphase flow simulations against the experimental results for both structured and random packed columns using MEA. The reactive multiphase flow simulations using volume of fluid method were conducted at a wide range of liquid loads and contact angles. The effective area is one of the critical factors dictating interphase mass transfer due to chemical reactions. Accordingly, CFD-predicted effective areas were compared with the experimental results of Tsai et al. [1] for Mellapak 250.Y structured packing. Both results matched well at different liquid loads in the presence of fast chemical kinetics using caustic solvents. Further, reactive multiphase flow simulations were also conducted in pall ring random packing to compute effective areas in the presence of fast chemical reactions. The CFD-predicted effective area compared well with correlation developed by Song et al. [2]. Based on the validations outlined in this report the simulation framework can next be used for predicting the hydrodynamics and mass transfer phenomena for CO₂BOL and other advanced solvents. The predictive models could also be used in the design optimization of the packed column. In addition to validation of the CFD model, this report also explains the mechanism for enhanced liquid side mass transfer for a structured packed column as compared to a wetted-wall column.

1.0 Background

The capture and storage of CO₂ from coal-fired power sources has the potential to reduce global emissions by 20% [4]. Post-combustion capture is the most popular configuration for CO₂ capture, because existing fossil-fuel power plants can be retrofitted to include CO₂ capture technology [5]. Solvent absorption by countercurrent flow in a packed column is a promising technology for mitigating CO₂ emissions from power plants [6-8]. The structured/random packing used in the packed column provides a large surface area for mass transfer while minimizing pressure drop across the column [9]. Before deploying this technology to industry, its performance and scalability must be investigated [10]. Accordingly, hydraulic characteristics and mass transfer between flue gas and liquid solvent phases in the packing system need to be better understood for optimal packing design. It is a challenging problem because of the large number of factors that influence the hydrodynamics and mass transfer behavior, such as solvent properties, surface characteristics, packing design, and liquid loading [11]. In this view, understanding the local hydrodynamics and mass transfer behavior is important because it reflects the liquid flow pattern within the column that significantly influences the overall mass transfer rate between phases.

This report describes the development of the computational framework for three-dimensional reactive multiphase flow simulations in the packed columns. The absorption of CO₂ using monoethanolamine (MEA) and caustic (NaOH) solvents is demonstrated for future flow predictions with other solvents, such as CO₂ binding organic liquids (CO₂BOL) in the packed columns. The methodology and mathematical formulations are briefly presented in Section 2. The mechanism for enhanced liquid side mass transfer in the packed column is presented in Section 3. Sections 4 and 5 describe the computational fluid dynamics (CFD) models for structured and random packed column and validations, respectively. The last section summarizes the outcome of the current work.

2.0 Methodology

2.1 Mathematical Formulations

Multiphase flow simulations for hydrodynamics and species transport in a representative elementary unit (REU) of Mellapak 250.Y structured packing were performed using the volume of fluid method (VOF) method [1]. The governing equations are as follows:

$$\nabla \cdot \mathbf{u} = 0, \quad (1)$$

$$\frac{\partial(\rho \mathbf{u})}{\partial t} + \nabla \cdot (\rho \mathbf{u} \mathbf{u}) = -\nabla p + \mu \nabla \cdot (\nabla \mathbf{u} + (\nabla \mathbf{u})^T) + \rho \mathbf{g} + \mathbf{F}, \quad (2)$$

Where p is the pressure, and \mathbf{g} is gravity. \mathbf{F} is a singular force raised due to interfacial surface tension that produces a jump in the normal direction across the interface. The terms ρ and μ are phase average density and viscosity, respectively, and are computed as follows.

$$\left. \begin{aligned} \rho &= \rho_g + \alpha(\rho_l - \rho_g) \\ \mu &= \mu_g + \alpha(\mu_l - \mu_g) \end{aligned} \right\} \quad (3)$$

Here, α is the volume fraction of secondary phase and suffices l and g denote the liquid and gas phase, respectively. The conservation Eqs. (1) and (2) are solved using the VOF method [1], which allows the entire flow field to be treated as a single phase. The surface tension force (\mathbf{F}) that appeared at the gas-liquid interface is implemented by continuous surface force model (CSF) [2]:

$$\mathbf{F} = \sigma \frac{\rho \kappa \nabla \alpha}{\frac{1}{2}(\rho_g + \rho_l)} \quad (4)$$

where σ is the interfacial tension, κ is the local curvature of the interface, and $\nabla \alpha$ presents direction vector. The curvature κ is computed by the divergence of the unit normal $\hat{n} = \nabla \alpha / \|\nabla \alpha\|$.

$$\kappa = \nabla \cdot \hat{n} \quad (5)$$

The interface where two fluids meet the wall is computed by wall adhesion and the contact angle (γ). The normal vector at the interface is adjusted near the wall by the following equation:

$$\hat{n} = \hat{n}_{wall} \cos \gamma + \hat{t}_{wall} \sin \gamma \quad (6)$$

where \hat{n}_{wall} and \hat{t}_{wall} are the unit vectors normal and tangential to the wall, respectively.

The interface between the phases is captured by solving the additional transport Eq. (7) for scalar α whose value varies from 0 to 1.

$$\frac{\partial \alpha}{\partial t} + \nabla \cdot \mathbf{u} \alpha + \nabla \cdot \mathbf{u}_c \alpha (1 - \alpha) = 0 \quad (7)$$

Here, u_c is sharpening velocity computed as $C \times |\mathbf{u}| \frac{\nabla \alpha}{|\nabla \alpha|}$, C is sharpening factor. The last term in the Eq. (7) is artificially introduced that acts against the interface smearing and assures the shape interface. Note that it only acts in the vicinity of interface, and, therefore, does not significantly affect the solution in the rest of the flow domain. In the case of two-phase simulation, Eq. (7) is solved only for the secondary phase, and volume fraction of the primary phase is computed as $(1 - \alpha)$.

2.2 Species Transport Equation

The single fluid formulation for mass transfer between two phases developed by Haroun et al. [3, 4] and Marschall et al. [5] are used in the flow simulations. It is capable of simulating species transfer across interfaces having arbitrary morphology using interface capturing methods, such as the VOF method. In this method, a single set of scalar transport equations is solved for the entire flow field.

$$\frac{\partial C_i}{\partial t} + \nabla \cdot (\mathbf{u} C_i - D_i \nabla C_i) = S_i \quad (8)$$

Here, C_i and D_i are the concentration and diffusivity of the i^{th} species. S_i is the species source term that accounts for the production of the i^{th} species due to chemical reactions. The computation for the source term was followed by the method explained by Wang et al. [6].

$$S_i = r \alpha C_s C_{CO_2} \quad (9)$$

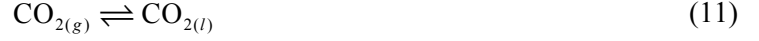
Here, r is reaction rate constant (will be explained later) and C_s is the concentration of solvent ($S \approx [\text{OH}^-]$ and RNH_2 in case of absorption via caustic and MEA solvent respectively). The previous reactive multiphase flow investigations using the VOF method conducted by Wang et al. [6] were performed in a 2D rectangular flat channel that mimics the wetted wall column. Because of the smaller flat domain, meshing was not a challenging issue in their study. In contrast, meshing is one of the major challenges in the present study due to the 3D corrugation sheet. One needs micron-sized mesh near the interface in the reactive mass transfer problem, which is not affordable in the 3D simulation of structured packing. Equation (9) was modified by introducing an additional polynomial factor presented in Eq. (10).

$$S_i = r \alpha^a (1 - \alpha)^b C_s C_{CO_2} \quad (10)$$

The additional factor was expected to overcome the impact of slightly coarser mesh near the interface. The value of the exponential factors a and b was calibrated against experimental data. The above expression (10) was incorporated as a source term in the Star-CCM+ via Field function.

2.3 Reaction Chemistry for Absorption of CO₂ in Aqueous NaOH Solution

The effective area (interfacial area) in the packed column was computed via Danckwerts method [7], which is based on absorption of CO₂ into caustic solvent sodium hydroxide (NaOH). The rate of reaction for absorption of CO₂ in caustic solvent is very fast and considered to be an instantaneous reaction [8]. Under this condition, mass transfer due to physical absorption is negligible as compared to a corresponding one due to chemical reaction [9]. Therefore, mass transfer due to reaction kinetics is only for accounted in the flow simulations. The reactions involved in the chemical absorption are as follows:



The rate of the reaction (13) is significantly higher than the rate of reaction (12). Subsequently, the reaction (12) dictates the overall reaction and can be considered as the pseudo first-order irreversible reaction [8].



The rate of reaction can be expressed as:

$$r = k_{\text{OH}^-} [\text{OH}^-] [\text{CO}_2] \quad (15)$$

Here, k_{OH^-} is the second-order reaction rate constant. At a very small concentration of CO_2 and superfluous amount of hydroxide ion, the reaction (15) can be treated as the pseudo first-order reaction. Accordingly, the concentration of $[\text{OH}^-]$ in the source term of Eq. (10) was kept constant. The rate constant can be written as

$$r \cong k_1 [\text{CO}_2] \quad (16)$$

where k_1 is the first-order reaction rate constant given as $k_1 = k_{\text{OH}^-} [\text{OH}^-]$. The value of the reaction rate was computed using the correlation developed by Pohorecki and Moniuk [8].

$$\left. \begin{aligned} \log_{10} \left(\frac{k_{\text{OH}^-}}{k_{\text{OH}^-}^\infty} \right) &= 0.221I - 0.016I^2 \\ \log_{10} k_{\text{OH}^-}^\infty &= 11.895 - \frac{2382}{T} \end{aligned} \right\} \quad (17)$$

Here, I is ionic strength of the solvent, and T is absolute temperature. Further, the overall mass transfer coefficient was computed using the correlation developed by Pohorecki and Moniuk [8].

$$k'_g = \frac{\sqrt{k_{\text{OH}^-} [\text{OH}^-] D_{\text{CO}_2,l}}}{H_{\text{CO}_2}}$$

Here, H_{CO_2} is Henry constant and $D_{\text{CO}_2,l}$ is diffusivity of CO_2 in liquid.

2.4 Reaction Kinetics for Absorption of CO_2 in Aqueous MEA Solvent

As mentioned earlier, the aqueous VOF method solutions of MEA are the most commonly used solvents for CO_2 capture via absorption due to high reaction rates [10]. However, reaction kinetics for absorption of CO_2 in MEA solvent are complex and not fully understood in spite of significant investigations. The majority of work assumes the reaction proceeds through a zwitterion mechanism [7, 11]. The zwitterion

mechanism was originally proposed by Caplow [11], but became popular after its reintroduction by Danckwerts [7]. The reaction between CO_2 and MEA ($\text{R}_1\text{R}_2\text{NH}$, here R_1 is $-\text{C}_2\text{H}_2\text{OH}$ and $\text{R}_2 = -\text{H}$) is assumed to be a two-step mechanism [7, 12]. The first step of the reaction involves the formation of a zwitterion.



The next step is formation of carbamate by removal of the proton by a base (such as amine, H_2O , OH^- , etc.)



Most of the absorber operates at low CO_2 loading, and the zwitterion formation is rate controlling. The concentration of the bicarbonates and carbonates are not significant in such conditions. The second step reaction (19) is ionic and virtually instantaneous. The overall reaction can be treated as an irreversible second-order reaction. The second-order reaction rate constant (k) is characterized by the temperature-dependent rate expression given by Hikita et al. [13].

$$\log_{10} k = 10.99 - 2152/T \quad (20)$$

Here, k has unit of *liter/gmol.s* and T is the absolute temperature in K .

2.5 Numerical Scheme

Reactive multiphase flow simulations were conducted using Star-CCM+ 12.0 [14]. The unsteady flow simulations were conducted via implicit transient formulation. The high-resolution interface capturing (HRIC) was used in the discretization in the interface, which is suitable for tracking the sharp interface [15]. Velocity and pressure are coupled using the segregated model. The momentum equation is solved in each direction separately. The linkage between the momentum and continuity equations is achieved with a predictor-corrector approach based on a Rhie-and-Chow-type pressure-velocity coupling combined with a Semi-Implicit Method for Pressure-Linked Equations (SIMPLE) algorithm [16]. The second-order upwind scheme was used in the spatial discretization of all equations. The simulation employed an implicit solution scheme in conjunction with an algebraic multigrid method (AMG) for accelerating convergence of the solver. Convergence of the solution was assumed when the sum of normalized residual for each conservation equation was less than or equal to 10^{-3} . In addition to that, simulations were terminated when the concentration of the CO_2 at the outlet and inlet was nearly constant. A very small variable time step ($\sim 10^{-5}$ sec.) was used in the simulation to satisfy the Courant–Friedrichs–Lewy (CFL) condition (Courant number = 0.50) for stability. Consequently, flow simulations become computationally expensive.

3.0 Direct Effect of Solvent Viscosity on the Physical Mass Transfer in a Packed Column

3.1 Introduction

Mass transfer between phases is a critical factor dictating the overall efficiency of the packed column employed in absorption, distillation, and extraction industries. Indeed, it governs the size of the column. The mass transfer in the packed column is a complex phenomenon that depends on the various factors such as solvent properties, local hydrodynamics, reaction kinetics, etc. The liquid flow pattern within the column significantly influences the overall mass transfer rate. In this context, understanding the mass transfer phenomenon is required for performance improvement of a packed column.

A number of experimental and theoretical studies have been conducted to explain the mechanism for mass transfer in structured packings. Various theories, including two-film theory [17], penetration theory [18], surface-renewal theory [19], and boundary-layer theory are applied to explain the mass transfer in a packed column. Most of the models for physical mass transfer are based on the two-film theory, which only considers the molecular diffusion in stagnant films that form each side of the gas-liquid interface [17]. On the other hand, Higbie's penetration theory [18] considers the residence time of a fluid element at the interface. It suggests an elementary idea to account for turbulence in mass transfer phenomena. Subsequently, correlation for the mass transfer coefficient is derived in terms of various dimensionless numbers, such as Reynolds, Schmidt, Froude, or Galileo number. Previously, the wetted wall column (WWC) concept was adopted to predict mass transfer based on the assumption of a well-defined geometry and precise surface area in the structured packings. However, recent investigations have shown complex flow behavior inside the packed column along with the presence of different flow morphologies. As a result, the mass transfer prediction significantly deviates from the WWC. The mass transfer between phases is dictated by many factors. Surface tension was proposed to have a negligible effect on mass transfer in the turbulent wavy film flow [20]. On the other hand, viscosity is one of the critical factors affecting the mass transfer phenomenon. A large value of solvent viscosity can lead to a significant reduction in the mass transfer coefficient. High solvent viscosity can slow diffusion of gas through the gas-liquid interface (indirect effect) and modify the local hydrodynamics by generating a more stabilized liquid film on the packing surface (direct effect). As a result, mass transfer across the interface can be significantly reduced.

The effect of viscosity on the mass transfer coefficient has been investigated in detail over the last few decades. Rochelle and his coworkers [21-25] have performed extensive experimental studies examining the performance evaluation of structure/random packings. The effects of various factors impacting the mass transfer area [23-25] and mass transfer coefficients between phases [21, 22] also have been extensively investigated. Song et al. [21, 22] have experimentally investigated the physical mass transfer for various carbon capture packings. The effect of viscosity on the overall mass transfer coefficient has been explained in two parts: (1) direct contribution due to hydrodynamics and (2) indirect impact that accounts for solvent diffusivity. An experimental campaign designed to study these factors could be expensive and time-consuming. Conversely, CFD simulations may be leveraged in the design process to achieve economic and efficient solutions while providing important insights into the physics. Notably, CFD does not replace the need for measurements, but it may diminish the amount of experimentation required and complement the setup and analysis. In addition, CFD steadily has been gaining acceptance for studying the flow characteristics in structured packings over time [26-30].

Haroun et al. [3, 4] and Marschall et al. [5] have developed the single fluid formulation for mass transfer between two phases. It is capable of simulating species transfer across interfaces having arbitrary morphology using interface capturing methods, such as the VOF method. To capture the concentration

jump across the interface, both approaches used Henry's law with a constant coefficient for thermodynamic equilibrium of chemical species. This approach also is employed [9, 31-33] for various chemical processes where mass transfer is important. Nieves-Remacha et al. [31] use this approach to simulate the hydrodynamics and mass transfer phenomenon in advanced-flow reactor technology, an alternative to scale-up continuous-flow chemistries from micron to millimeter scales. Hu et al. [34] have conducted a VOF simulation similar to the method suggested by Haroun et al. [4] for mass transfer in a falling wavy film. They characterize the CO₂ absorption mass transfer in vorticity in the vicinity of the interface and the local CO₂ concentration. In the same context, Singh et al. [35, 36] have conducted VOF simulations for film and rivulet flow over an inclined plate for the shape gas-liquid interface and flow morphology. Extensive multiphase flow simulations also have been conducted that account for the factors affecting rivulet shape and stability. Note that the shape of the interface significantly affects the mass transfer across it. Sebastia-Saez et al. [37] have investigated physical mass transfer in a countercurrent flow over an inclined plate. Mass transfer due to physical absorption shows non-monotonic variation with increased liquid load. The maximum value of mass transfer is observed at the fully wetted film. Recently, Chao et al. [32, 33] have applied a similar approach for physical and reactive mass transfer for CO₂ capture in a WWC, where they show the advantage of CFD modeling over the standard two-film theory. In addition, CFD modeling can account for local flow hydrodynamics, such as wavy interface, and variation in film thickness in CO₂ capture. Haroun et al. [4] shows that mass transfer between phases strongly depends on the packing design. A sheet of triangular channel shows higher mass transfer than a flat surface. However, their problem setup was limited to concurrent gas-liquid flow.

In a recent experimental study by Song et al. [22], the direct effect of viscosity on the mass transfer coefficient is shown to be significantly higher than the corresponding one for a WWC. The mass transfer coefficient for a WWC was derived by Pigfor [21] and can be expressed as:

$$k_L = 1.15 \cdot u_L^{0.333} \nu_L^{-1/6} g^{1/6} \left(\frac{a^{1/3}}{L^{1/2}} \right) D_L^{1/2}, \quad (21)$$

where u_L is solvent velocity at the inlet, ν_L is the kinematic viscosity, g is the gravitational acceleration, D_L is the diffusivity of the transport species in the solvent phase, a is the solvent inlet size, and L is the WWC height. This analytical expression (21) was derived via solving the hydrodynamic equations for laminar film falling over a vertical plate coupled with mass transfer in accordance with the penetration theory [38, 39]. On the other hand, a similar correlation was derived from extensive experimental outcome for the packed columns [22]:

$$k_L = 0.12 \cdot u_L^{0.565} \nu_L^{-2/5} g^{1/6} a_p^{-0.065} D_L^{1/2}, \quad (22)$$

where a_p is a specific area of the packings presented as m²/m³. Equation (22) clearly shows a higher impact of solvent viscosity on the mass transfer coefficient for a packed column with an exponent of $-2/5$ as compared to $-1/6$ for the WWC (Eq. (21)). In addition, a larger dependence of mass transfer on the solvent velocity (u_L) also can be identified for the packed column with an exponent of 0.565 compared to 0.33 in Eq. (21). Of note, the flow in a packed column is more complicated compared to WWCs because of various factors, including the intermittent nature of the liquid distributor, surface characteristics of the packing material, and the turbulent nature of flows due to design and arrangement of packing units. As a result, flow in the packed column significantly deviates from a well-controlled laminar flow found in the WWC. Subsequently, it may contribute to the enhanced dependency of mass transfer on the viscosity [22]. However, unlike the analytical expression for WWC (Eq. (21)) that is corroborated by a rigorous and quantitative theory, the exact mechanism is not fully understood for the packed column, and associated quantitative analysis is still lacking. In this context, an extensive theoretical study with numerical

simulations will provide significant insights and quantitative explanations of the physics behind the correlation in Eq. (22), as well as additional insights into the design optimization of a packed column.

3.2 Mathematical Formulation of the Physical Mass Transfer

We consider a wavy film with rolling waves falling over a vertical flat plate due to gravity with the physical mass transfer of gas species across the gas-liquid interface. Figure 1 shows the schematic of the problem, where rolling waves can be characterized by an amplitude A , wavelength λ , and wave speed u_w . As a result, the thickness profile $\delta(x, t)$ of the wavy film varies vertically in the falling direction. The x -axis is directed downward in the streamwise direction (see Figure 1), and the y -axis is perpendicular to the plate. The governing (continuity and momentum conservation) equations dictating the falling film are given as:

$$\frac{\partial u}{\partial x} + \frac{\partial v}{\partial y} = 0, \quad (23)$$

$$\frac{\partial u}{\partial t} + u \frac{\partial u}{\partial x} + v \frac{\partial u}{\partial y} = -\frac{1}{\rho_L} \frac{\partial P}{\partial x} + \frac{\mu_L}{\rho_L} \left(\frac{\partial^2 u}{\partial x^2} + \frac{\partial^2 u}{\partial y^2} \right) + g, \quad (24)$$

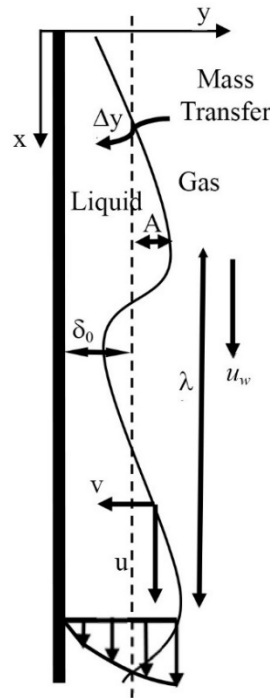


Figure 1. Schematic description of a wavy film falling over a vertical plate, where u and v are vertical and horizontal velocity, respectively. The falling film with an average thickness δ_0 can be described by a rolling wave with an amplitude A , a wavelength λ , and a wave speed u_w .

$$\frac{\partial v}{\partial t} + u \frac{\partial v}{\partial x} + v \frac{\partial v}{\partial y} = -\frac{1}{\rho_L} \frac{\partial P}{\partial y} + \frac{\mu_L}{\rho_L} \left(\frac{\partial^2 v}{\partial x^2} + \frac{\partial^2 v}{\partial y^2} \right), \quad (25)$$

where u and v are the vertical and horizontal components of the velocity, ρ_L is the liquid density, μ_L is the dynamic viscosity, and P is the pressure. A parabolic velocity profile in the streamwise direction for u may be established across the film, which is based on the exact solution of a steady and fully developed laminar film flow [40]:

$$u(x, y) = \frac{3q}{2w} \left(\frac{2y}{\delta^2(x)} - \frac{y^2}{\delta^3(x)} \right). \quad (26)$$

Here, w is the width of film along the direction perpendicular to the x-y plane, and q is the flow rate,

$$q = w \int_0^{\delta(x)} u(x, y) dy = w \cdot u_{av}(x) \delta(x), \quad (27)$$

where $u_{av}(x)$ is the average vertical velocity at a location x . Using Eq. (26), the gradient of vertical velocity u in the x direction can be related to the local film thickness $\delta(x)$,

$$\frac{\partial u}{\partial x} = \frac{\partial u}{\partial \delta} \frac{\partial \delta}{\partial x} = -\frac{3q}{2w} \frac{y}{\delta^4} (4\delta - 3y) \frac{\partial \delta}{\partial x}. \quad (28)$$

The gradient of lateral velocity v along the y direction at the interface can be computed using the continuity Eq. (23)

$$\left. \frac{\partial v}{\partial y} \right|_{y=\delta(x)} = - \left. \frac{\partial u}{\partial x} \right|_{y=\delta(x)} = \frac{3q}{2w} \frac{1}{\delta_0^2} \frac{\partial \delta}{\partial x}, \quad (29)$$

where δ_0 is the average film thickness that can be written as

$$\delta_0 = \left(\frac{3\mu_L^2 \text{Re}}{\rho_L^2 g} \right)^{1/3} \quad (30)$$

according to the Nusselt theory [41]. Here, Re is the film Reynolds number defined as,

$$\text{Re} = \frac{\rho_L q}{\mu_L w} = \frac{q}{\nu_L w} = \frac{u_L a}{\nu_L}, \quad (31)$$

where a is the size of the solvent inlet, u_L is the solvent velocity at inlet, and ν_L is the kinematic viscosity of the solvent. For a turbulent wavy film flow, transport near a gas-liquid interface is governed by eddies whose length and velocity scales are characterized by bulk turbulence [20, 42]. According to the mixing length model for eddy diffusion [43], the eddy diffusivity stemming from the local turbulent flow in the direction normal to the vertical plate can be written as:

$$D_{Le} = C_1 \cdot \left| \left. \frac{\partial v}{\partial y} \right|_{y=\delta(x)} \right| (\Delta y)^2. \quad (32)$$

Here, C_1 is a proportional constant, Δy is the penetration depth of gas species into the solvent during a single wave period $T = \lambda/u_w$ (shown in Figure 1). The penetration depth Δy depends on the wave

frequency f and can be related to the diffusivity of that species in liquid phase (D_L) and the frequency (f) of rolling waves,

$$\Delta y = \sqrt{D_L/f} = \sqrt{D_L \lambda/u_w}. \quad (33)$$

Substitution of Eqs. (29) and (33) into Eq. (32) leads to the expression for eddy diffusivity D_{Le} :

$$D_{Le} = \left[0.72 C_1 \frac{\partial \delta}{\partial x} f \left(\frac{\rho_L g^2}{\mu_L} \right)^{1/3} \text{Re}^{1/3} \right] D_L. \quad (34)$$

To determine D_{Le} , the thickness gradient $\partial \delta / \partial x$ and the wave frequency f need to be modeled explicitly. We assume that an arbitrary fluid element at the gas-liquid interface follows a random walk motion along the y direction (shown in Figure 1) due to the momentum transfer. The velocity of that fluid element over a single period T of the rolling wave can be written as:

$$V_y = \sqrt{v_L \frac{u_w}{\lambda}} = \sqrt{v_L f}, \quad (35)$$

where, again, v_L is the kinematic viscosity; λ is the wavelength; u_w is the wave speed; and $f = u_w / \lambda$ is the wave frequency. Concurrently, the same fluid element also will experience downward motion along the x direction because of the gravity and vertical velocity gained during the same period T and can be written as:

$$V_x = g \frac{\lambda}{u_w} = \frac{g}{f}. \quad (36)$$

The gradient of film thickness along the x direction ($\partial \delta / \partial x$) can be approximated using the wave amplitude A and wavelength λ as:

$$\frac{\partial \delta}{\partial x} \approx \frac{2A}{\lambda}. \quad (37)$$

A and λ can be related to the distance that the fluid element travels in vertical and lateral directions in a single rolling wave period T . These two quantities should be proportional to the speed in both directions and can be written as:

$$\frac{1}{2} \frac{\partial \delta}{\partial x} \approx \frac{A}{\lambda} = C_2 \frac{V_y}{V_x}, \quad (38)$$

Where C_2 is a dimensionless constant on the order of unity. To verify this relation, we use the results obtained from the nonlinear solution of the wavy film falling over a vertical plate by Shkadov [44]. The various optimum parameters of the wave regime, such as wavelength, wave propagation speed, and frequency, can be computed as a function of the Reynolds and Kapitza numbers (Ka), where Ka incorporates the effect of surface tension:

$$Ka = \frac{\sigma}{\rho_L} \left(\frac{\rho_L^4}{g\mu_L^4} \right)^{1/3} = \frac{\sigma}{\rho_L} \left(\frac{1}{g\nu_L^4} \right)^{1/3}, \quad (39)$$

Where σ is the surface tension. In Figure 2, we plot the variation of the computed value of A/λ with V_y/V_x at three given Reynolds numbers with the Kapitza number varying between 400 and 4000. It can be observed that the variation of A/λ with V_y/V_x remains unchanged for all Reynolds and Kapitza numbers studied. Furthermore, it clearly shows the linear scaling relation as $A/\lambda = C_2 V_y/V_x$ with $C_2 \approx 0.67$. The numerical solutions [44] are in good agreement with our projection (Eq. (38)) and confirm that the ratio between wave amplitude and wavelength is proportional to the ratio of two velocity components gained during a single wave period T .

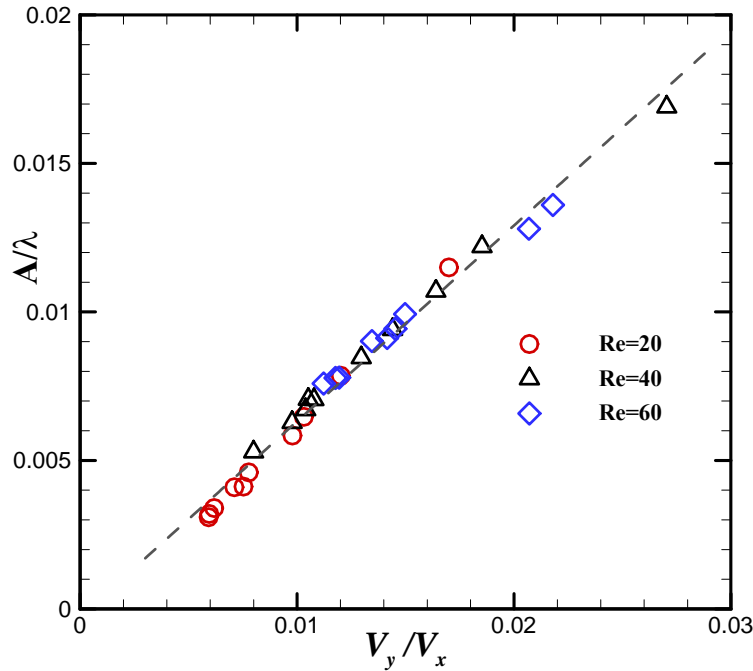


Figure 2. Variation of normalized wave amplitude (A/λ) with ratio of wave velocity components (V_y/V_x) at different Reynolds numbers. It shows the linear scaling ($A/\lambda \sim V_y/V_x$) and independence of Reynolds number.

Next, the ratio A/λ can be plotted as a function of Reynolds and Kapitza numbers using the same solution methods [44],

$$\frac{A}{\lambda} = C_3 Ka^{-n} Re^m. \quad (40)$$

Here, C_3 is another dimensionless constant. In Figure 3(a), we present the variation of A/λ with Reynolds number Re . As expected, A/λ increases with an increased value of Re . Conversely, A/λ decreases with an increased value of Ka , which is shown in Figure 3(b) for two different Reynolds numbers. Physically, it can be understood by the fact that the increased value of the Kapitza number leads to a reduction in film thickness and an increase in wavelength. Subsequently, fluctuations in film thickness also decrease, causing a lower value of A/λ . Both observations also are confirmed in the numerical simulations and will be explained in a later section (Figures 6 and 7). Accordingly, A/λ decreases with the increased value of Ka .

In addition, A/λ shows nonlinear variation with Re and Ka . To find the scaling relation for the variation of A/λ with Re and Ka , nonlinear regression is conducted, and a scaling relation $A/\lambda = C_3 Re^{0.78} Ka^{-0.47}$ is observed (shown in Figure 4) with $C_3 \approx 1/60$, with $m \approx 3/4$ and $n \approx 3/7$.

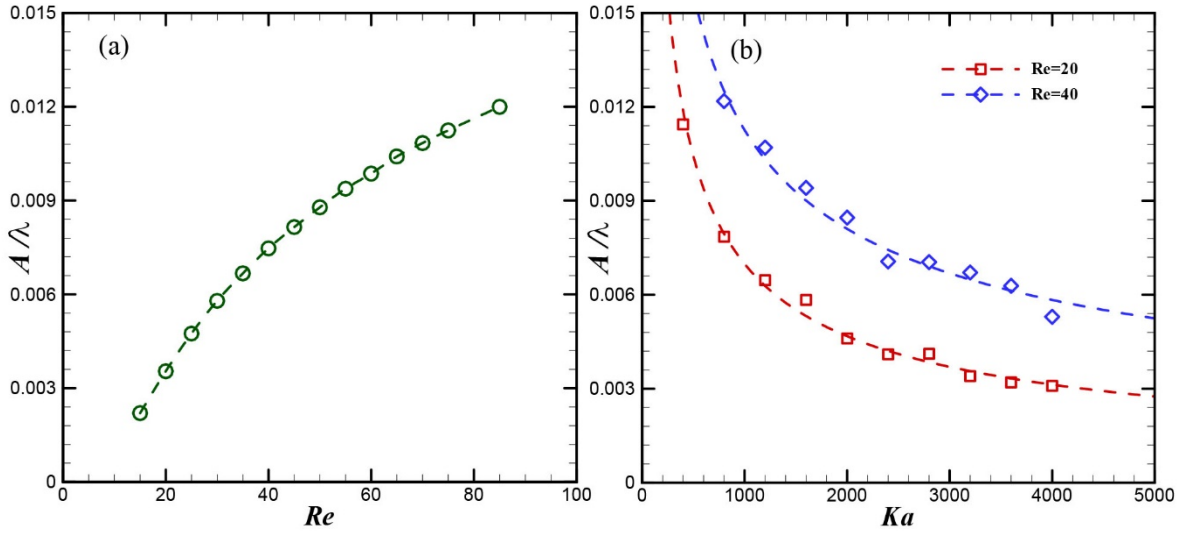


Figure 3. (a) Variation of the normalized wave amplitude (A/λ) with Reynolds number at $Ka=2850$. (b) Variation of (A/λ) with Ka at two Reynolds numbers shows that normalized amplitude decreases with increased Kapitza number.

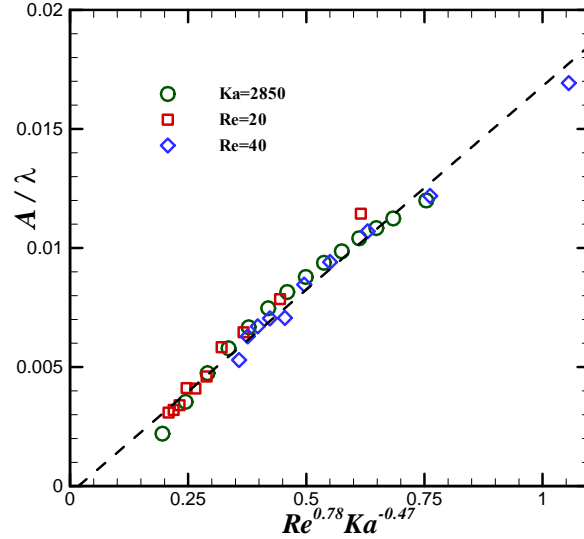


Figure 4. Variation of normalized wave amplitude with Reynolds and Kapitza numbers shows the scaling $A/\lambda \sim Re^{0.78} Ka^{-0.47}$. The exponents of the fitting for Re and Ka reasonably match the previous studies by Shkadov [44].

Finally, we can write these relations together as:

$$\frac{1}{2} \frac{\partial \delta}{\partial x} \approx \frac{A}{\lambda} = C_2 \frac{V_y}{V_x} = C_2 \frac{\sqrt{v_L}}{g} f^{3/2} = C_3 Ka^{-n} Re^m. \quad (41)$$

Substituting Eq. (41) into Eq. (34), the final expression for the eddy diffusivity for wavy film flow with rolling waves can be presented as:

$$\begin{aligned} D_{Le} &= 1.44 \left[C_1 \cdot C_2 \left(\frac{V_y}{V_x} \right)^{1/3} Re^{1/3} \right] D_L \\ &= 1.44 C_1 \cdot C_2^{2/3} C_3^{1/3} Re^{(m+1)/3} Ka^{-n/3} D_L \\ &= C Re^{(m+1)/3} Ka^{-n/3} D_L \end{aligned} \quad (42)$$

Here, $C = 1.44 C_1 C_2^{2/3} C_3^{1/3}$ is another empirical constant that aggregates three constants together. To derive the expression for effect of viscosity on the mass transfer coefficient in a wavy film flow with rolling waves, the molecular diffusivity D_L in the analytical expression for WWC (Eq. (21)) can be replaced by the eddy diffusivity D_{Le} . The difference in mass transfer between wavy film and uniform film flow is assumed to be primarily due to the difference in diffusivity. It generates the following expression:

$$\begin{aligned} k_{Le} &= 1.15 u_L^{1/3} \left(\frac{\mu_L}{\rho_L} \right)^{1/6} g^{1/6} \left(\frac{a^{1/3}}{L^{1/2}} \right) D_{Le}^{1/2} \\ &= 1.15 u_L^{1/3} \left(\frac{1}{v_L} \right)^{1/6} g^{1/6} \left(\frac{a^{1/3}}{L^{1/2}} \right) C^{1/2} \left(\frac{u_L a}{v_L} \right)^{(m+1)/6} \left(\frac{\sigma}{\rho_L} \left(\frac{1}{v_L^4 g} \right)^{1/3} \right)^{n/6} D_L^{1/2} \\ &= 1.15 C^{1/2} u_L^{(3+m)/6} g^{(3-n)/18} \left(\frac{a^{(3+m)/6}}{L^{1/2}} \right) \left(\frac{\sigma}{\rho_L} \right)^{n/6} v_L^{-(6+3m+4n)/18} D_L^{1/2} \end{aligned} \quad (43)$$

The original expression for WWC (Eq. (21)) can be fully recovered by substituting the value of the constant $C = 1$, exponents $m = -1$, and $n = 0$ in Eq. (43). However, in the case of a packed column, these values can differ because of the turbulent wavy nature of flow. From the solutions of wavy film flow with rolling waves, we find the exact values of exponents as $m \approx 3/4$ and $n \approx 3/7$ that can be estimated from the scaling relations (Eq. (40)), shown in Figure 4.

Substituting the value of exponents of m and n into Eq. (42), the eddy diffusivity can be related to the Reynolds number (Re) and Kapitza number (Ka)

$$D_{Le} = C Re^{7/12} Ka^{-1/7} D_L, \quad (44)$$

and the corresponding mass transfer coefficient (k_{Le}) can be expressed as:

$$\begin{aligned}
k_{Le} &= 1.15C^{1/2}u_L^{5/8}g^{4/21}\left(\frac{a^{5/8}}{L^{1/2}}\right)\left(\frac{\sigma}{\rho}\right)^{-1/14}v_L^{-61/168}D_L^{1/2} \\
&= 1.15C^{1/2}u_L^{0.625}g^{0.19}\left(\frac{a^{0.625}}{L^{0.5}}\right)\left(\frac{\sigma}{\rho}\right)^{-0.07}v_L^{-0.36}D_L^{1/2}
\end{aligned} \tag{45}$$

The preceding expression for effective mass transfer coefficient is based on the coupling of hydrodynamic equations and eddy diffusion. It can be quantitatively compared to the correlation derived from extensive experiments for a packed column (Eq. (22), repeated here for convenience),

$$k_L = 0.12 \cdot u_L^{0.565} g^{0.17} a_p^{-0.065} v_L^{-0.4} D_L^{0.5} . \tag{46}$$

It is clear that the mass transfer coefficient for wavy film has significantly higher dependence on both the solvent flow rate and viscosity compared to the uniform film flow in a WWC (Eq. (21)). This dependence matches well with the correlation (Eq. (46)) developed from an experimental investigation for a packed column [22]. The expression presented in Eq. (45) confirms the functional form of the correlation derived from the experimental observations (Eq. (46)) with a slight difference in the exponent values. The proposed mechanism, i.e., enhanced diffusivity due to wavy film flow in a packed column, reasonably captures the deviation of physical mass transfer from the WWC. Furthermore, the present expression for the mass transfer coefficient explores additional contributions from interfacial surface tension. Note that this term is missing in the experimentally derived correlation (Eq. (46)), which highlights the impact of surface tension on the hydrodynamics, thereby influencing the mass transfer phenomena. While it may be minor for an aqueous amine-based solvent, it can be more significant for a solvent with a higher value of interfacial surface tension.

Moreover, the mass transfer coefficient can be normalized by $D_L/(v_L^2/g)^{1/3}$, where the term $(v_L^2/g)^{1/3}$ is the viscous length scale. A similar method also has been applied earlier by Yih [42]. The normalized mass transfer coefficient (k_{Le}^*) depends on several dimensionless numbers:

$$k_{Le}^* = \frac{k_L}{D_L} \left(\frac{v_L^2}{g} \right)^{1/3} = 1.15C^{1/2} \cdot \text{Re}^{(3+m)/6} \text{Sc}^{1/2} \text{Ka}^{-n/6} \text{Ga}^{-1/6} . \tag{47}$$

Here, $\text{Sc}=v_L/D_L$ is the Schmidt number, and $\text{Ga}=gL^3/v_L^2$ is the Galileo number. In the case of a WWC, the normalized mass transfer coefficient can be obtained by substituting the value as $C=1$, $m=-1$, and $n=0$ in Eq. (47):

$$k_{L(WWC)}^* = 1.15 \cdot \text{Re}^{1/3} \text{Sc}^{1/2} \text{Ga}^{-1/6} . \tag{48}$$

Therefore, enhancement in the mass transfer for a wavy film can be expressed as:

$$E = \frac{k_{Le}^*}{k_{L(WWC)}^*} = C^{1/2} \text{Re}^{(1+m)/6} \text{Ka}^{-n/6} . \tag{49}$$

A greater enhancement in the mass transfer can be expected for a large Reynolds number and small Kapitza number because $m > 0$ and $n > 0$ for a wavy film flow with rolling waves.

3.3 Problem Setup

The unsteady flow simulations are conducted using Star-CCM+12.0 [45] based on the implicit transient scheme. In the implicit approach, the specified time step involves inner iterations to converge the solution. The integration scheme marches inner iterations using pseudo-time steps according to specified values of the Courant number for stable and converged solutions. The segregated solver was used that solves each of the momentum equations in turn, one for each dimension. The coupling between the momentum and continuity equations is achieved with a predictor-corrector approach based on the Rhie and Chow interpolation method in conjunction with the SIMPLE algorithm [16] for pressure-velocity coupling. The second-order upwind scheme is used in the spatial discretization of all equations. An implicit solution scheme is used in conjunction with an AMG for accelerating convergence of the solver.

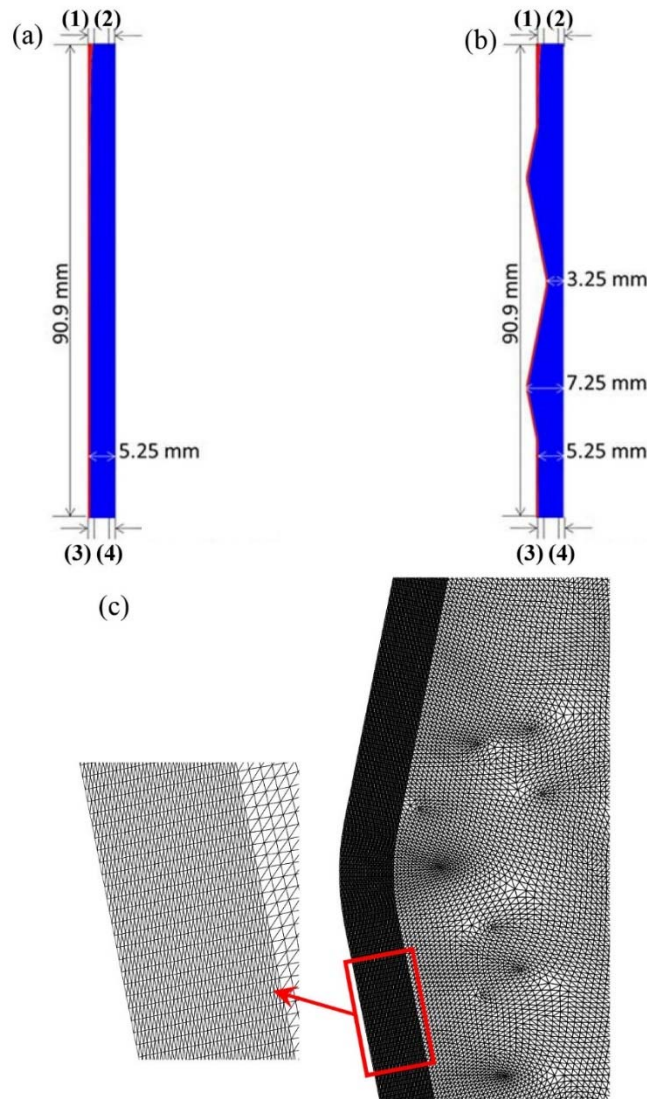


Figure 5. Schematic of flow domain showing the inlet and outlet positions for both phases: (a) wetted wall column and (b) zigzag column as 2D representative of structured packings. The inlet and outlet of both phases have 1 mm width. (c) The dark region at the left in the exploded view of the discretized domain shows very fine mesh to capture the mass transfer phenomenon.

We have investigated the influence of solvent viscosity on the mass transfer for both wavy film flow with rolling waves and uniform film flows in a WWC and a zigzag column (ZZC). The periodic wavy film is introduced via periodic perturbations at the solvent inlet. The WWC geometry is chosen from the previous study of Wang et al. [32, 33]. The ZZC is selected for its 2D representation of structured packed columns. A similar approach also has been considered earlier for 2D representation of the structured packed column for investigating the hydrodynamics of countercurrent flow [28, 29]. Figure 5 depicts the schematic of the WWC and ZZC designs and their corresponding parameters. Both columns are placed vertically, and gravity acts in a downward direction. Dimension (height and width) of the WWC and ZZC geometries are kept the same to compare the mass transfer coefficient for both cases. The inlet and outlet of the gas and liquid phases have 1 mm widths. This inlet and outlet size is selected based on a previous WWC study [33].

The computational flow domain is developed and meshed in Star-CCM⁺. To accurately and efficiently capture the mass transfer phenomenon, the domain is discretized using very fine mesh. The mesh density proximate to the left wall where liquid falls appears finer than in the adjacent region for the surrounding gas. A more refined mesh also is required in the inflexion region near the zigzag channel apex to capture the flow behavior (see the exploded view of dark region of the mesh domain in Figure 5c). For numerical simulation of diffusive mass transfer, grid size near the interfacial region needs to be lower than the mass diffusion length scale ($\sqrt{4D_L t}$). The exposure time (t) was calculated from the interfacial velocity (maximum velocity) and height of the column. The grid size near the film region was chosen to be 25 μm , which is lower than the minimum diffusion length scale (27 μm). Therefore, the grid size was assumed to be sufficient for the flow simulation. Because of the very small grid size, flow simulations require a tiny time step ($\Delta t \sim 10^{-6} - 10^{-5}$ sec) to satisfy the CFL condition for stability with a Courant number = 0.50. As a result, flow simulations become quite expensive computationally.

Countercurrent flow simulations have been conducted for the multicomponent gas (air and nitrous oxide, N_2O) and amine-based solvents ($\rho_L = 1058 \text{ kg/m}^3$) as working fluids. The solvent viscosity is varied over a wide range ($\mu_L \sim 1 - 10 \text{ cP}$) to investigate its direct impact on the mass transfer between two phases. The gas phase has a density of (ρ_g) 1 kg/m^3 and viscosity (μ_g) of 0.015 cP . The diffusivities of N_2O in the air and solvent are specified as $D_G = 1.67 \times 10^{-5} \text{ m}^2/\text{s}$ and $D_L = 1.3 \times 10^{-9} \text{ m}^2/\text{s}$, respectively. The solvent enters the domain at the top (1) and exits the bottom (3) because of gravity. Both uniform (0.17 m/sec) and oscillating velocity profiles [$0.17(1 + 0.05\sin 2\pi\omega) \text{ m/sec}$ and $\omega = 60\text{Hz}$] are prescribed at the solvent inlet to introduce the flat film flow and wavy film flow, respectively. On the other hand, uniform gas inlet velocity (0.049 m/sec) with N_2O concentration of 13.31 mol/m^3 is specified at the bottom (see gas inlet (4) in Figure 5 (a and b)). The outlet of both phases is specified as a pressure outlet with zero gauge pressure. The remaining boundaries, including zigzag sheet, are defined as a no-slip wall with a static contact angle (γ) of 70° . The benchmark results correspond to fixed liquid flow rates. In that case, a flow rate of $u_L = 0.17 \text{ m/s}$ and $u_G = 0.049 \text{ m/s}$ ensure a stable film flow with a smooth interface for a flat surface. The simulation cases are summarized in Table 1.

Table 1. Details of the cases in flow simulation.

Viscosity (cP)	Wetted Wall Column		Zigzag Column	
	Flat film with uniform flow rate	Wavy film with oscillating flow rate	Flat film with uniform flow rate	Wavy film oscillating flow rate
1 ~ 10	UWWC	OWWC	UZZC	OZZC

OWWC = oscillatory inlet in wetted wall column
OZZC = oscillatory inlet in zigzag column
UWWC = uniform film flow in WWC
UZZC = uniform film flow in ZZC

3.4 Results and Discussion

Analytical and numerical studies have been conducted for the mass transfer via physical absorption in a countercurrent gas-liquid flow. To explain its impact on the mass transfer coefficient, the flow simulations have been conducted for a range of solvent viscosity (1–10 cP) for uniform and oscillating inlet flow. In the simulations, we only consider the direct effect of solvent viscosity that affects the hydrodynamics. The indirect impact of viscosity on the mass transfer coefficient via viscosity-dependent diffusivity is not included, which involves the relations between diffusivity and viscosity of the solvents. The simulated results are presented in terms of dimensionless numbers: Reynolds, Kapitza, Schmidt, and Galileo numbers. These numbers already are defined in the previous section.

3.4.1 Film Thickness

A thin film facilitates the mass transfer between the gas and liquid phases, and the mass transfer coefficient strongly depends on the film thickness. In addition, it also dedicates the heat transfer between the solvents and wall. In this context, computation of the film thickness is performed first. The effect of viscosity on the film thickness is presented in terms of Kapitza number, a dimensionless number that depends only on the solvent properties. Figure 6(a) shows the variation of film thickness with viscosity for a uniform film flow in WWC and ZZC (UWWC and UZZC). As expected, film thickness increases with increased viscosity for both cases. The predicted value of the film thickness (δ) matches well with the corresponding value computed from the Nusselt theory [41]. A slight discrepancy in the value of film thickness is observed at low viscosity ($\mu \leq 2$ cP). This may be due to the triangular shape of the channel that causes little instability in the film flow. The film velocity accelerates at the tip and retards in the trough region to satisfy flow continuity. However, the magnitude of the discrepancy in the film thickness is considered to be negligible. At higher viscosity, both show almost the same δ value. Note that the damping of turbulent eddies within the liquid film near both the liquid and solid surface is governed mainly by viscosity [42]. Subsequently, a smooth and uniform film appears in both cases (UWWC and UZZC).

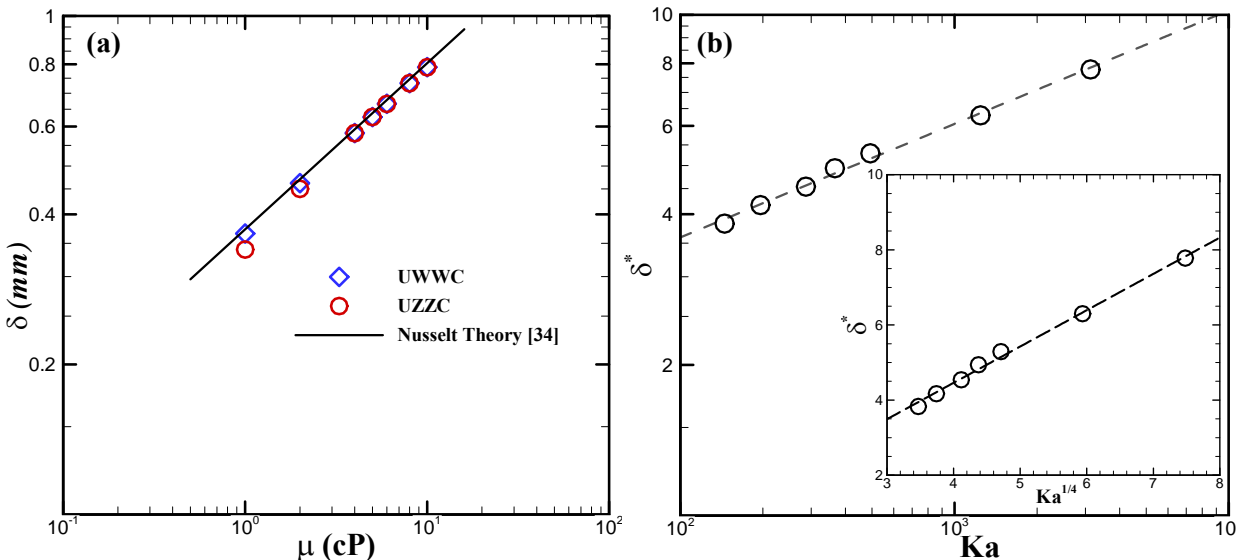


Figure 6. (a) Plot shows variation of the film thickness (δ) with solvent viscosity (μ) for the WWC. Predicted value of the film thickness matches well with Nusselt theory [34]. (b) Variation of the normalized film thickness with Kapitza number. Inset of (b) shows the scaling relation of $\delta^* \sim \text{Ka}^{1/4}$.

Next, the film thickness is normalized by the viscous length scale as $\delta^* = \delta/(v_L^2/g)^{1/3}$. Figure 6(b) shows the variation of δ^* with the Kapitza number for a UWWC. The normalized film thickness increases with an increased Kapitza number. However, the absolute value of the film thickness varies the other way, i.e., decreases with the increased value of the Kapitza number. Note that a higher value of the Kapitza number corresponds to a lower value of solvent viscosity. It also shows a scaling relation $\delta^* \sim Ka^{1/4}$. Earlier, Singh et al. [35] presented similar scaling for film falling over an inclined plate. Film thickness also has been reported to increase with solvent viscosity [35, 46], which is consistent with the Nusselt theory [41]. As mentioned earlier, film stability is governed by the competing effects between various forces acting on it. At high viscosity, enhanced viscous forces act against gravity and make the film more stable [26]. As a result, film thickness increases.

As already mentioned, flow simulations have been conducted for the oscillating inlet. Because of the oscillating inlet velocity, a wavy film appears. Wang et al. [33] observe that wavelength (λ) of the wavy film decreases with increased frequency (f) for oscillatory inlet in wetted wall columns (OWWCs). The pronounced impact of the frequency is visible at $f = 60$ Hz. Accordingly, $f = 60$ Hz is chosen in the flow simulations for all viscosities. The wavelengths of the wavy film are computed and compared for both WWCs and ZZCs. The computed value of the wavelength also can be normalized as $\lambda^* = \lambda/(v_L^2/g)^{1/3}$. Figure 7 shows the variation λ^* with Ka . As expected, the normalized wavelength increases with the increased value of the Kapitza number for both cases. Note that the lower value of Kapitza number corresponds to higher viscosity. As noted, viscosity stabilizes the film and acts as damping factors for the wave. Furthermore, the normalized wavelength λ^* value is almost the same for both cases, except a slight discrepancy is observed at a higher value of the Kapitza number.

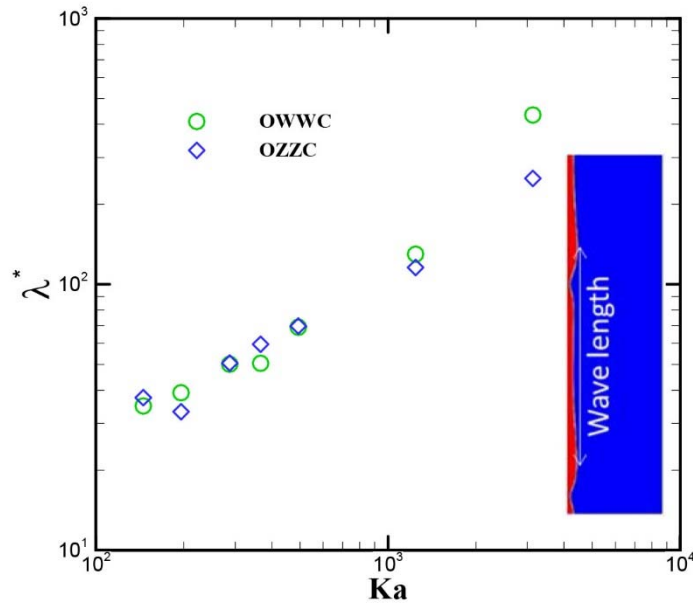


Figure 7. Plot shows variation of the normalized wavelength (λ^*) in a periodic wavy film with Kapitza number (Ka) for WWC and ZZC. Inset shows the wavy film (red color) and method to compute wavelength.

3.4.2 Mass Transfer Coefficient

In this section, we consider the mass transfer from gas to liquid phase due to physical absorption. The 2D simulation using the VOF method of co-current gas-liquid flow in the structure packed column is conducted

to compute the interfacial mass transfer [9]. The mass transfer is not directly affected by the recirculation in the liquid side under corrugation cavities. Indeed, the chemical species only penetrate in a very thin concentration layer. Thus, the transfer process is controlled by the diffusion/advection at the film interface.

The methodology for computing the mass transfer coefficient is the same as in Wang et al. [33] and is only briefly presented here. The mass transfer coefficient (k_L) for physical transport via absorption is calculated using standard formula

$$k_L = j / \Delta p, \quad (50)$$

where j is the mass transfer flux ($\text{mol}/\text{m}^2 \cdot \text{s}$) at the gas-liquid interface and ΔP is the driving force computed as:

$$\Delta P = \frac{P_{N_2O,in} - P_{N_2O,out}}{\ln\left(\frac{P_{N_2O,in}}{P_{N_2O,out}}\right)}. \quad (51)$$

Applying the ideal gas law, ΔP can be written in terms of the concentration of the N_2O at the gas inlet and outlet:

$$\Delta P = \frac{(C_{N_2O,in} - C_{N_2O,out})RT}{\ln\left(\frac{C_{N_2O,in}}{C_{N_2O,out}}\right)}, \quad (52)$$

where R is the ideal gas constant ($\text{J}/\text{K} \cdot \text{mol}$) and T is the temperature in the unit of K. To compare the numerically computed value of the mass transfer coefficient with an analytically calculated one, the unit of the mass transfer is converted to m/s .

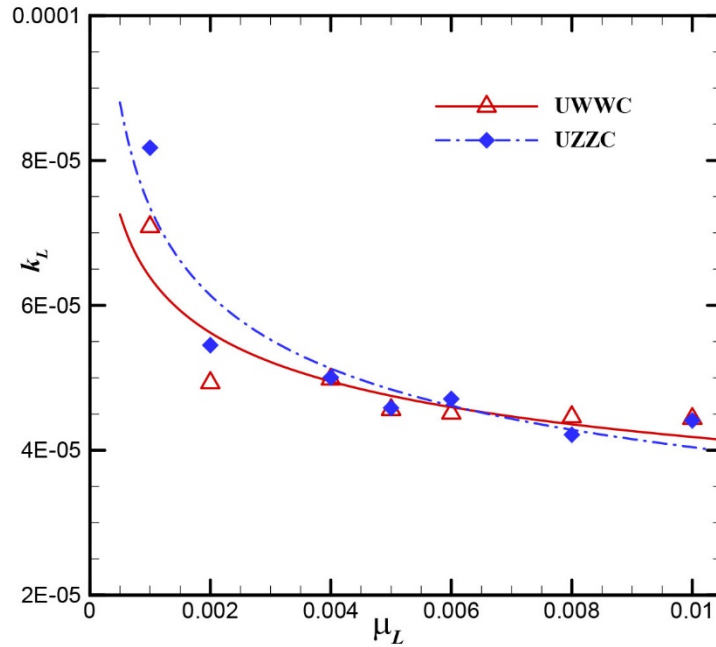


Figure 8. Variation of the mass transfer coefficient (k_L) with solvent viscosity (μ_L) wetted wall column and zigzag column in the case of a smooth and uniform film.

Figure 8 shows the variation of the mass transfer coefficients with viscosity for uniform inlet velocity (UWWC and UZZC) of $u_L = 0.17$ m/sec. The UZZC shows higher mass transfer coefficient (especially at small viscosity) when compared to the WWC. This effect is due to the packing geometry and can be explained by the flow field in the packed column in Figure 9. Note that hydrodynamics plays a critical role in the mass transfer. In Figure 9, the recirculation zones are seen in the gas side for the UZZC. The recirculation zone enhances the convection. Previous studies by Haroun et al. [3] also uncovered a similar observation. The mass transfer is found to be higher for a triangular channel compared to a corresponding one for a flat liquid film.

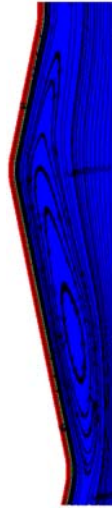


Figure 9 Exploded view in the triangular channel shows velocity streamline and concentration distribution in the flow domain. It also illustrates the recirculation zones on the gas side due to triangular geometry.

Figure 10 shows the variation of k_L with solvent viscosity for both flat and wavy film flow. As expected, the mass transfer coefficient decreases with increased solvent viscosity in all four cases. Here, wavy film flow shows steep variation with viscosity. The difference between k_L for wavy and smooth film is observed to be higher at lower viscosity. At higher viscosity, the difference becomes smaller. Increased value of viscosity damps the initial perturbation in the flow field. On the other hand, interfacial surface tension and gravitational forces dominate the viscous force at small viscosity. As a result, eddies at the interface occur and promote the mass transfer and higher interfacial area. In Figure 11(a), we compare the variation of the mass transfer coefficient with viscosity for expression (45) and numerically compute one at a fixed solvent and gas flow rate and wide range of viscosity ($\mu \sim 1 - 10$ cP), where $C = 0.115$ corresponds to the WWC. The value of C might be different for the structured packed column where flow is generally considered to be more chaotic. Both plots match reasonably well, except the analytically derived expression shows slightly steep variation, i.e., higher exponent value (-0.36). In addition, the scaling for k_L with solvent viscosity shows a scaling relation $k_L \sim \nu_L^{-0.34}$ for a wavy film in the OWWC (see Figure 11(b)). This is nearly the same as the exponent value -0.36 in Eq. (45), as well as the experimental observation (-0.4 in Eq. (46)) by Song et al. [21, 22].

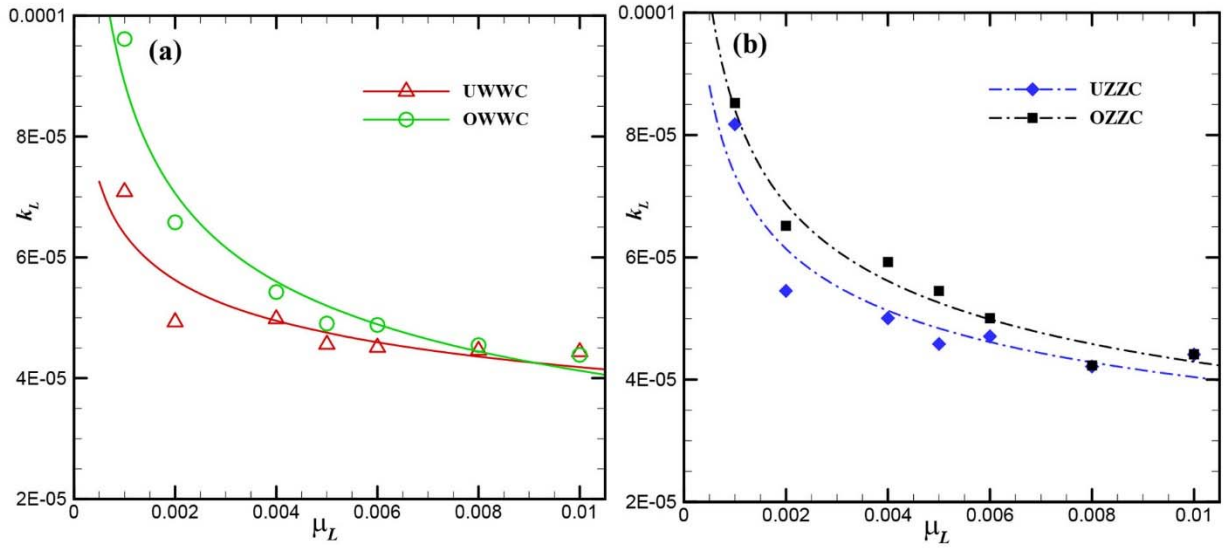


Figure 10. Variation of the mass transfer coefficient (k_L) with solvent viscosity (μ_L) for smooth and wavy film flow in: (a) wetted wall column and (b) zigzag column. Prefix U: Uniform and O: Oscillatory Inlet.

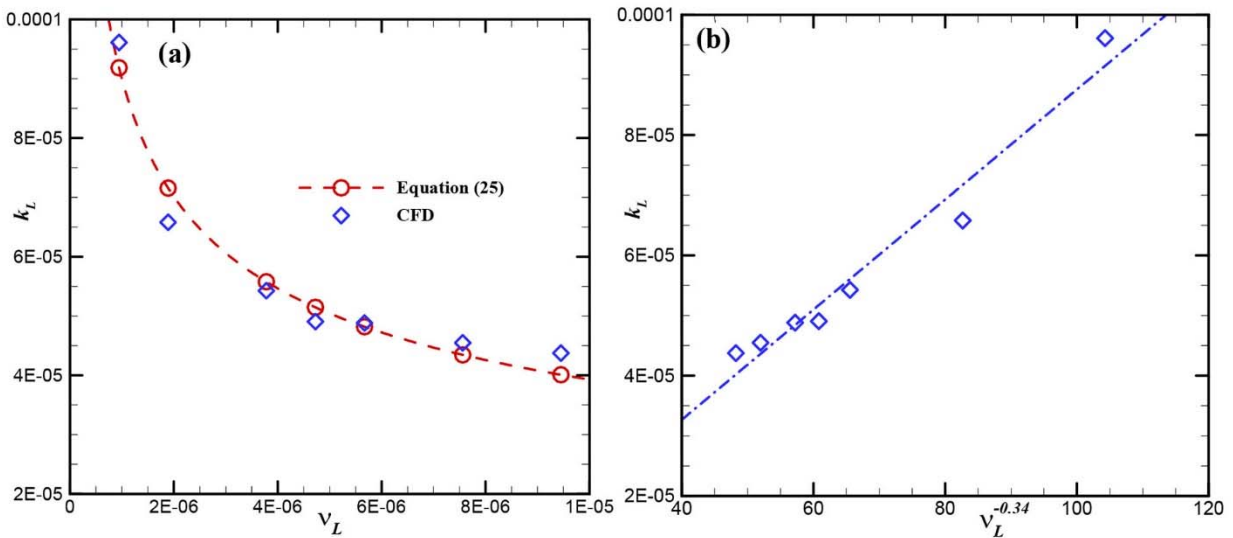


Figure 11. (a) Comparison of the variation of the mass transfer coefficient with solvent viscosity for analytically derived expression (Eq. 25) and CFD simulations for OWWC. Both reasonably show the same trend of the variation of mass transfer coefficient with viscosity. (b) Variation of the mass transfer coefficient (k_L) with solvent viscosity (ν_L) shows a scaling $k_L \sim \nu_L^{-0.34}$ for OWWC.

4.0 Multiphase Flow Investigations in the Structured Packings

4.1 Introduction

Structured packed column has been extensively used in chemical industries for distillation and absorption processes for the last couple of decades. The absorption is carried out via countercurrent gas-liquid flow in the column. It has been preferred over the random packed column because it provides a larger interfacial area with minimum pressure drop across the column. Apart from distillation and process industries, it has been recently considered as a prospective technology for mitigating the greenhouse gas emission from power plants. However, development of the technology for carbon capture via solvent absorption is at the nascent stage. Few attempts have been made either in the pilot scale or small plant scale such as Mongstad in Norway (300,000 tons/year CO₂ capture) and Boundary Dam Sask Power in Canada (1 M tons/year CO₂ capture). Before its deployment in commercial scale, performance evaluation and scalability at large-scale need to be evaluated. The performance of the column depends on both hydrodynamic and mass transfer phenomena. For example, liquid maldistribution can significantly deteriorate separation efficiency [47]. Note that these parameters depend on many factors such as solvent properties (surface tension and viscosity), packing surface characteristics (contact angle, roughness), packing design, liquid load, etc. [35]. Experimental investigations for studying impacts of these factors independently might be very expensive and time-consuming. On the other hand, CFD simulation can provide economic and efficient solutions, thereby complementing the experiments. Subsequently, CFD has gained substantial attention for studying the flow characteristics in structured packings over the past couple of decades. A structured packed column exhibits wide variation in length scales: column dimension ($\phi \sim 5\text{--}10$ m and $h \sim 20\text{--}30$ m), dimensions of packing unit (~ 20 cm), and film thickness (< 1 mm). These scales cannot be resolved in a single computational model. Therefore, a multiscale modeling approach is suggested to overcome the disparities in length scales [48]. It can provide useful insights into the hydrodynamics of the packing unit, which is focused on the study of effective mass transfer area in a packed column.

A number of 3D CFD investigations were conducted for single-phase [49], pseudo-single-phase, and two-phase flow study in the structured packings. Multiphase flow simulations using the VOF method were conducted for liquid falling over an inclined plate to explain the wetting of the packed column [35, 50]. The concept of flow over an inclined plate was also employed to derive models for hydrodynamic parameters such as liquid holdup [51] and interfacial area in structured packings. 3D single-phase flow simulations were conducted by Owen et al. [49] and found good matching of CFD-predicted dry pressure drop with experimental ones for Mellapak N250.Y packings. Later, the pseudo-single-phase approach was adopted for wet pressure drop calculation in the packed column [28, 29]. In these studies, film thickness was computed in 2D simulations to derive liquid holdup for the calculation of wet pressure drop via the pseudo-single-phase approach in 3D simulations. As noted earlier, interfacial area is a critical factor for absorption efficiency, and numerous experimental and computational efforts were reported.

Computational studies using the VOF method were focused on the wetting of a single corrugated sheet for point inlet [52-54] as well as inlet throughout the sheet [55]. Subramanian and Wozny [54] examined the rivulet flow over a single corrugated sheet; however, different fluids and contact angles were involved in the simulation and the effects of the solvent properties could not be assessed independently. Flow between two corrugated sheets was also performed by Shojaee et al. [56] and Subramanian and Wozny [54]. Shojaee et al. [56] calculated wet pressure drop and interfacial area in Gempak 2A packing. The interfacial area was not calculated directly but rather via the average value of film thickness and liquid holdup. Furthermore, VOF simulations were focused on the REU of the packed columns [57-59]. Ataki and Bart [26] conducted flow simulations in REU of Rombopack packing to explain the effects of solvent properties on wetting, and

proposed a correlation for the interfacial area and liquid holdup. Haroun et al. [58] also used the VOF method to investigate the hydrodynamics in REU of Mellapak 250.X. The REU consists of four periodic repeating units. The effects of solvent flow rate and contact angle on the interfacial area were investigated. Basden [57] used the same methodology to investigate the interfacial area and liquid holdup in the REU of packings. The effect of different parameters affecting hydrodynamics were studied; however, studies were not systematic and complete. Recently Sebastia-Saez et al. [59] also investigated the mesoscale model based on REUs of the MontzPak B1-250 packings for computation of the liquid holdup and the interfacial area. However, realistic boundary condition was used in the simulation, and subsequently their observations for interfacial area may be uncertain. Tsai et al. [23] showed that solvent viscosity has a negligible effect, whereas surface tension marginally affects the interfacial area. Rizzuti and Brucato [60] showed non-monotonic variation of the interfacial area with viscosity; that is, the interfacial area increases and then decreases with increasing viscosity.

Wetting of the column is strongly tied to surface characteristic of the packing [61]; i.e., contact angle and surface texture. The contact angle is a characteristic for solid-liquid systems in a specific environment [62], and a solvent can exhibit different values of contact angle depending on the solid surface. A lower value of contact angle shows more hydrophilic characteristics, and subsequently, leads to enhanced interfacial area [35, 63]. In addition, the surface texture was found to promote wetting in the packed column [24, 64] by reducing the value of contact angle [65, 66]. Effects of the surface tension were excluded in the studies [58, 59]. The recent studies for falling liquid over an inclined plate [35], as well as for a single corrugated sheet [53], have shown that the impact of contact angle on the interfacial area ties with surface tension of liquid at a given flow rate. Effects of contact angle on the interfacial area were found [63, 67] to be pronounced for a solvent having lower surface tension value. Nevertheless, most of the empirical models for interfacial area [24, 68] proposed in the past assumed uniform distributed and fully wetted flow pattern in each section of packing, thereby undermining the effects of contact angle. Furthermore, models developed by Rocha et al. [69] and Gualito et al. [70] overweigh the impact of contact angle. Both models were derived by adding an adjusting parameter in the Shi and Mersmann model [63], which was originally developed via 1D model for liquid falling over an inclined plate. Indeed, some models [71-75] did not account for surface tension in the derivation of models, whereas surface tension is a critical factor dictating the liquid spreading over a solid surface.

The wetting of the packing surface in the structure packed column is quite complex and is not yet fully understood. Few attempts were made to explain the local hydrodynamics in the packed column accounting for all physical properties and solid surface characteristics. In addition, available data are also restricted to small viscosity, particularly in the range of viscosity of MEA. Currently, a highly viscous solvent, CO₂BOL, is being developed as a prospective solvent for carbon capture via the absorption process. Data for such highly viscous liquids are scant; therefore, extensive flow investigations are required to understand the hydrodynamic characteristics before industrial deployments. As proposed in the proposal, device-scale multiphase flow models using the VOF method are being developed and validated against experimental results for effective mass transfer area using caustic (NaOH) and aqueous amines. Effects of the liquid load, contact angle, and solvent properties on the effective area are being presented.

4.2 Problem Setup

We have conducted flow simulations for the computation of effective area in the REU of Sulzer Mellapak 250.Y packing. Similar to previous studies [57, 67], the computational model of the REU was prepared by perpendicular arrangement of two smooth corrugated sheets (see Figure 12). The REU of Mellapak 250.Y packings consists of a single repeating unit in the lateral direction and three units in the flow direction. According to industrial design of the packing unit, a 2 mm gap was provided between sheets. The design of the corrugated sheet is the same as the design specified by Sulzer, and perforation in the sheet was not

included in the modeling of flow domain. Previous studies of X-ray imaging performed by Green et al. [76] suggested that the liquid films cover perforations for the majority of liquid loads operated; eventually it would lead to minimal area loss. Therefore, results for sheets without perforation would not be significantly different than the corresponding results in the case of perforated sheets. A schematic of the computational flow domain is presented in Figure 13. The solvent enters in the flow domain through its top sheet and leaves from the bottom due to gravity (see Figure 13(a)). As per industrial design, a 2 mm gap was provided between sheets. In the simulation, the sheet was set as no-slip walls with the static contact angle. Both sides of the domain were specified as periodic boundary conditions that allow flow to cross and reenter in the flow domain through the lateral boundary (side walls). In some of the previous studies, symmetry boundary condition was used [59, 77] in a similar setup. Note that flow from a repeating unit passes to other ones as well. The symmetric boundary condition constraints flow inside the REU, which can be seen in Figure 4 of reference [59]. Therefore, this might not be a realistic condition for investigating such flow simulations. The liquid outlet and top faces were set to pressure outlets with zero gauge pressure. The uniform inlet velocity boundary conditions were specified for both liquid and gas phases. Positive and negative values of the velocity inlet were specified to impose countercurrent flows. A similar boundary condition for gas and liquid inlet was used previously [56, 58].

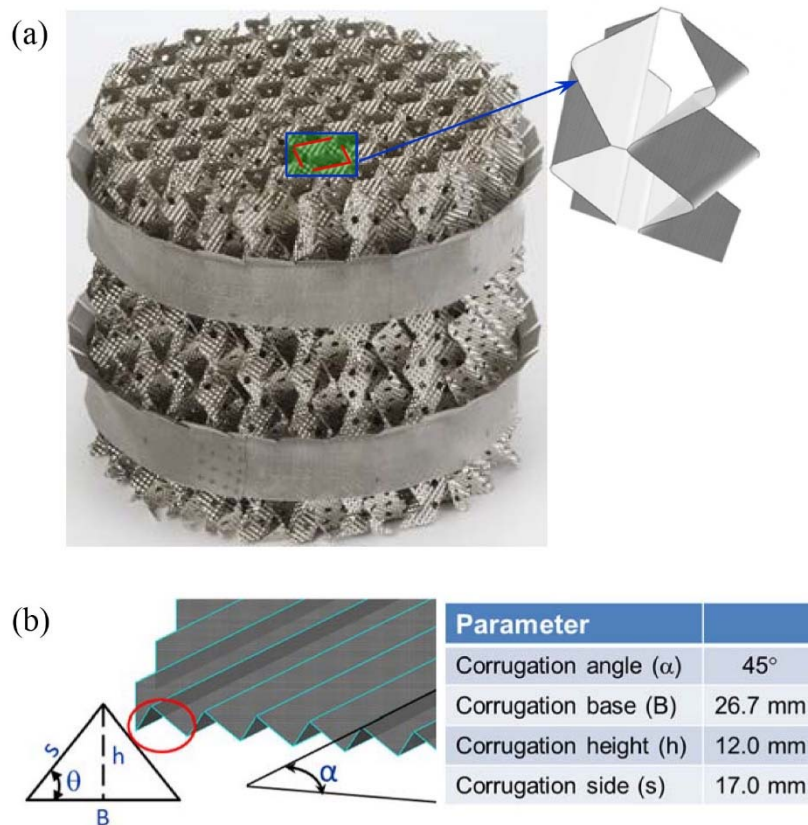


Figure 12. (a) An image of a typical structured packing shows the side-by-side arrangement of corrugated sheets. Exploded view explains the selection of current model in the flow simulations (Source: <https://www.sulzer.com>). (b) The corrugated sheet design used to construct the REU of Mellapak 250.Y structured packing for the CFD simulations.

Modeling the flow domain is challenging due to the complex geometry of the REU, in particular, corrugated sheets having triangular channels with corrugation angle. The model of flow domain was created in ‘Salome 8.3’, an open-source CAD software as per design of the sheet shown in Table 2. The model was exported

in the Star-CCM+ 12.0 for meshing and flow simulations. Meshing of the computational domain is a crucial step affecting stability and accuracy of the results. To capture the hydrodynamics and mass transfer phenomena accurately and efficiently, flow domain was discretized with non-uniform mesh. The mesh near the corrugated sheets was created finer using a prism layer scheme. In this region, liquid film appears, and mass transfer between phases occurs; consequently, it requires very fine mesh. Apart from this, the inflexion region near the apex of the triangular channel was also refined to capture the flow behavior. Therefore, minimum grid size as $25\ \mu\text{m}$ was specified in this region. Further, the gradient-based polyhedral mesh was used to discretize the remaining parts of the flow domain (see Figure 13(b)). Consequently, 4.09 M cell elements in the flow domain were arrived after grid independent tests, which will be discussed in a later section. Because of the very fine mesh, flow simulation required a short time step ($\Delta t \sim 10^{-5}$ sec.) to satisfy the CFL conditions according to value of the Courant number as 0.50. As a result, these simulations were computationally very expensive. A single flow simulation takes 4–7 days wall time depending upon solvent properties and contact angle using 120 cores to achieve pseudo-steady state on Constance, the Pacific Northwest National Laboratory (PNNL) supercomputer.

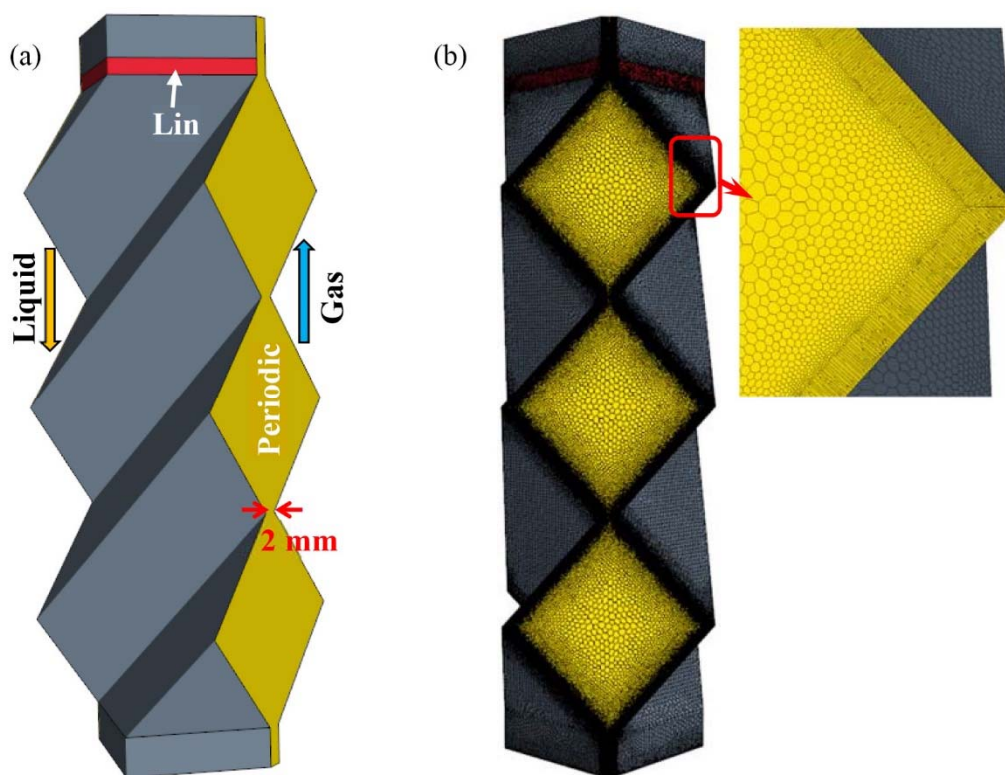


Figure 13. (a) 3D view of the computational flow domain of REU shows the countercurrent flow direction of gas and solvents. The periodic boundary is specified at the side of the domain. Liquid is introduced along the inner perimeter of the top and gas was fed from the bottom of flow domain. (b) Meshing of the flow domain shows the polyhedral cells used in flow domain and very fine mesh near the sheet where gas-liquid interface is expected to exist (see the exploded view).

Table 2. Design of the corrugated sheet used in Mellapak 250.Y.

Parameters	Dimension
Corrugation angle (α)	45°
Corrugation base (B)	26.70 mm
Corrugation height (h)	12.00 mm
Corrugation side (s)	17.00 mm
Specific area (a_p)	250 m ² / m ³
Void fraction (ϵ)	0.96

The reacting multiphase flow studies were conducted with flue gas ($\rho = 1.185 \text{ kg/m}^3$ and $\mu = 1.831 \times 10^{-5}$ Pas) and an aqueous solution of MEA at different concentrations as working fluids. The MEA is a more popular solvent and was selected for flow simulation. Gas was fed from the bottom and leaves from the top of the flow domain. Tsai et al. [24, 78] computed the gas side resistance using the correlation developed by Rocha et al. [79] for absorption of SO₂ into caustic solvents at four gas flow rates ($u_g = 0.60, 1, 1.5,$ and 2.3 m/sec.). The gas side mass transfer resistance was found to be 1–2% of the overall mass transfer resistance. Therefore, the gas side mass transfer resistance can be neglected and the overall mass transfer will be dominated by the liquid side. Accordingly, gas velocity was chosen as 1.0 m/sec. to ignore the gas side mass transfer resistance. The commercially employed solvents in the absorption process included aqueous solution of 0.10 M NaOH and MEA at two concentrations (0.30 and 0.40 fraction by mass). The values of the physical properties of these solvents are presented in Table 3. The value of contact angle (γ) for each solvent was not available. It would be worthy to note that the CO₂ absorption is carried out in the prewetted column. Because of the prewetted textured sheet, one can expect a lower value of the contact angle. Accordingly, a small value of contact angle was used ($\gamma = 10^\circ$) in the preliminary simulations. Note that the contact angle is a critical factor that significantly affects the wetting dynamics of a solvent for a given solid. Hence, its effects on the hydrodynamics were also extensively investigated.

Table 3. Physical properties of solvents used in flow simulations.

Solvent	μ_1 (mPas)	ρ_1 (Kg/m ³)	σ (mN/m)	k'_g	R
Water	0.89	997.0	72.80		
0.10 M NaOH	0.97	997.0	72.80	8.466	4.09×10^{-07}
30% MEA	2.457	1058	59.50	5.9636	1.67×10^{-06}
40% MEA	3.791	1053	54.80	5.9636	1.56×10^{-06}

% = percentage by weight, M = molar concentration

4.3 Results and Discussions

The results of flow simulations for the interfacial area are discussed for a wide range of solvent properties, flow rates, and contact angles. A number of commercially employed solvents in the absorption process are used as the liquid phase in simulations; therefore, it exhibits a wide range of variations in physical properties. In such cases, the Reynolds number is not a suitable dimensionless number as a representative of inertia. The Weber number appropriately represents the fluid inertia in this case and is used by others [24, 26, 50].

4.3.1 Comparison with Experiments at Different Liquid Loads

Preliminary flow simulations were conducted to validate CFD prediction that will show the reliability and accuracy of the numerical prediction. Accordingly, flow predictions are compared with those from experiments as a means to validate the present method for computation of effective area in Mellapak 250.Y structured packings with perforated sheet [78]. Tsai et al. [78] measured the effective area of Mellapak 250.Y structured packing having 0.46 m and 0.427 m outer and inner diameters, respectively. A 0.1M aqueous solution of NaOH was used as solvent. It was distributed using a pressurized fractal distributor with 108 drip points/m². Air was introduced from the bottom of the packing and air velocity was in the range of 0.50–1.50 m/s. During the experiment, CO₂ concentration at the gas inlet and outlet was monitored using the infrared gas analyzer. The liquid load was incremented, with a given liquid load being maintained until CO₂ concentration at the gas outlet achieves steady state. The column was prewetted via opening the top valve and subsequently circulating the solvent in the packed column for 15–30 minutes. More details of the experimental studies can be found somewhere else [78, 80].

CFD simulation was also conducted in line with experiments. Flow simulations were conducted for gas velocity of 1.0 m/sec. for 0.1M NaOH solution at different liquid loads. Due to the prewetted textured sheet, one can expected a lower value of the contact angle. Because of computational power restriction, the simulations were limited to a smooth surface. Note that surface texture/embossment has been reported to effectively reduce the contact angle, thereby promoting sheet wetting [65, 66]. Hence, a lower value of the static contact angle ($\gamma = 10^\circ$) was used in the flow simulations for mimicking experimental conditions. The flow simulations were run until a pseudo-steady state was achieved regarding the constant value of outlet and inlet flux of CO₂ (see Figure 14). The corresponding value of CO₂ flux was subsequently used to compute the effective area in the packed columns via Danckwerts method [7] as:

$$A_f = \frac{u_g}{k'_g ZRT} \ln \left(\frac{C_{CO_2,in}}{C_{CO_2,out}} \right) \quad (53)$$

Here, Z is the height of the column, R is the molar gas constant, and T is the temperature. Note that the above expression (53) was derived with simplification such as same area of inlet and outlet cross section, uniform gas velocity, etc. During the computation of effective area, flux of CO₂ was used instead of its concentration.

$$A_f = \frac{u_g}{k'_g ZRT} \ln \left(\frac{J_{CO_2,in}}{J_{CO_2,out}} \right) \quad (54)$$

Here, $J_{CO_2,in} = C_{CO_2,in} u_{g,in} A_{in}$ and $J_{CO_2,out} = C_{CO_2,out} u_{g,out} A_{out}$ are CO₂ flux at inlet and outlet respectively.

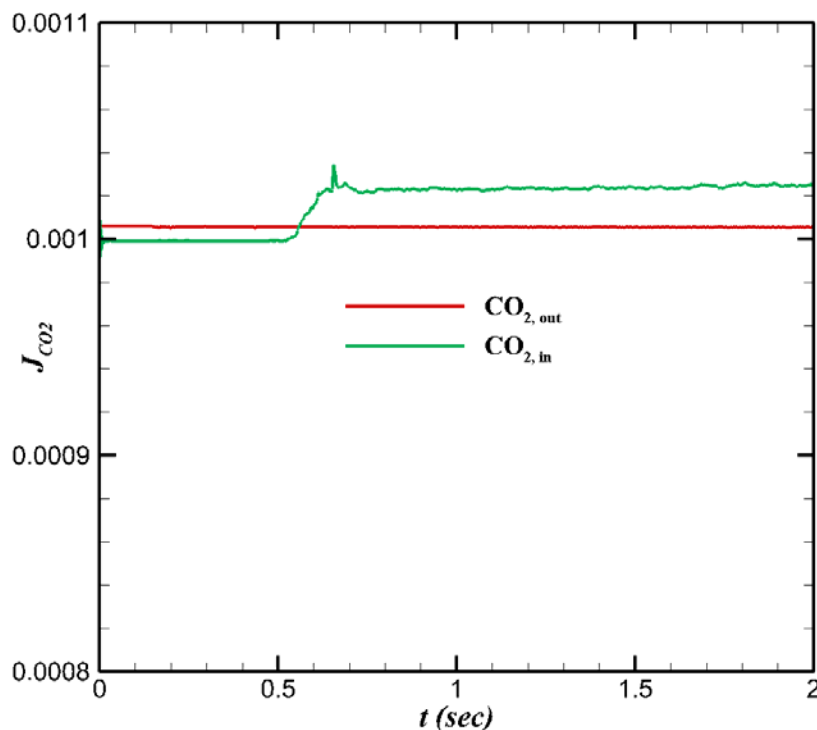


Figure 14. Temporal evolution of the CO₂ flux at the inlet and outlet of the flow domain. The pseudo-steady state was assumed when the CO₂ flux at the inlet and outlet remains constant.

The CFD-predicted effective area was computed using Eq. (54) for the gas velocity of 1 m/sec. Figure 15 shows the comparison between CFD-predicted effective area and the experiments. As expected, effective area increases with increasing liquid loads for both methods. The CFD-predicted effective area (A_{eff}) matches well with the corresponding one for experiments. A small discrepancy is found at lower liquid load; otherwise both show excellent matching.

Note that the effective area was indirectly measured via Denkwerts method [7]. On the other hand, CFD is also capable of directly measuring the effective area. Accordingly, it was calculated as the area of iso-surface and corresponds to $\alpha = 0.50$. The corresponding shape of the interface is shown in Figure 15(c). It would be worthy to note that the interfacial and wetted areas are different quantities. Wetted area is the area corresponding to solid-liquid interface (see Figure 15(b)). In principle, the interfacial area should be the same as the effective area because chemical reaction occurs at the gas-liquid interface. A similar approach was also adopted earlier for the computation of interfacial area [26, 53, 58, 67]. The computed value of interfacial area (A_I) was further normalized by the specific area of the packing (A_p) as $A_{I_n} = A_I/A_p$. The interfacial area shows a lower value than the effective area at all liquid loads in Figure 15(a). The discrepancy might be due to the value of mass transfer coefficient used in the computation of the effective area.

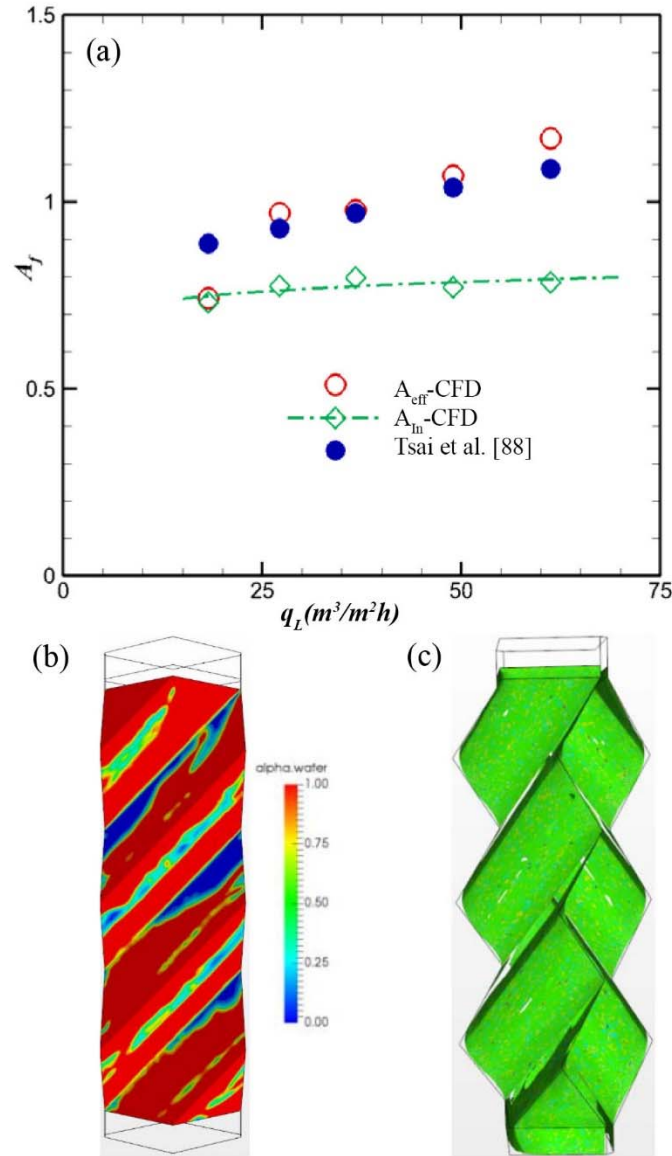


Figure 15. (a) Comparison of the CFD-predicted fractional area with experimental predicted area by Tsai et al. [80] at different liquid loads. Typical snapshots for (a) wetted and (c) interfacial area in the REU at $q_L = 49 m^3/m^2h$.

Note that the structured packed column shows a higher value of the mass transfer coefficient compared to the corresponding value in the case of wetted wall columns. In the computation of effective area, the theoretical value of the mass transfer coefficient was considered; consequently, a higher value of the effective area is observed. It would be worth noting that the VOF method has been successfully used in similar flow studies by many researchers for hydrodynamics [35, 36, 53, 67, 81] and for reactive mass transfer in a two-phase flow system [6, 9, 32, 33]. Therefore, it can be concluded that the VOF method is an appropriate method to investigate the reactive multiphase flow in a packed column.

4.3.2 Effect of Solvent Properties

In the previous section, 0.10 M NaOH was used as a solvent that has high surface tension and low viscosity. Note that the local hydrodynamics of the structured packed column strongly depend on physical properties of the solvent [35]. Hence, the simulation campaign was continued for other solvents, namely aqueous solution of MEA (30 and 40 by weights). However, highly viscous solvent CO₂BOL will be also used in the later stage as a major goal of the projects. As reported earlier [56], interfacial area is a critical factor dictating the mass transfer between phases in a solvent absorption system.

Figure 16 shows variation of the normalized interfacial area with liquid load for 30MEA and 0.10 M NaOH at $\gamma = 10^\circ$. As expected, interfacial area increases with increased liquid loads. Here, 30MEA shows a slightly higher value of interfacial area than the corresponding one for 0.10 M NaOH. Note that 30MEA has a higher value of viscosity but lower value of surface tension. It was noted earlier for wetting of the corrugated sheet that higher interfacial area was found at low Ka values corresponding to low surface tension and high viscosity [53]. In the wetting of a surface, surface tension plays a key role. Note that cohesion force weakens at a low σ value and adhesive force dominated. As a result, interfacial is found to be higher in the case of 30MEA. The previous studies by Tsai et al. [78] also found enhanced effective area (interfacial area) at the lower value of surface tension for Mellapak 250.Y. In contrast, Bravo and Fair [82] observed enhanced interfacial area with increasing value of surface tension in the random packing. A random packed column that has a different design and higher surface tension can form droplets and slender liquid ligaments. Subsequently, interfacial area might increase.

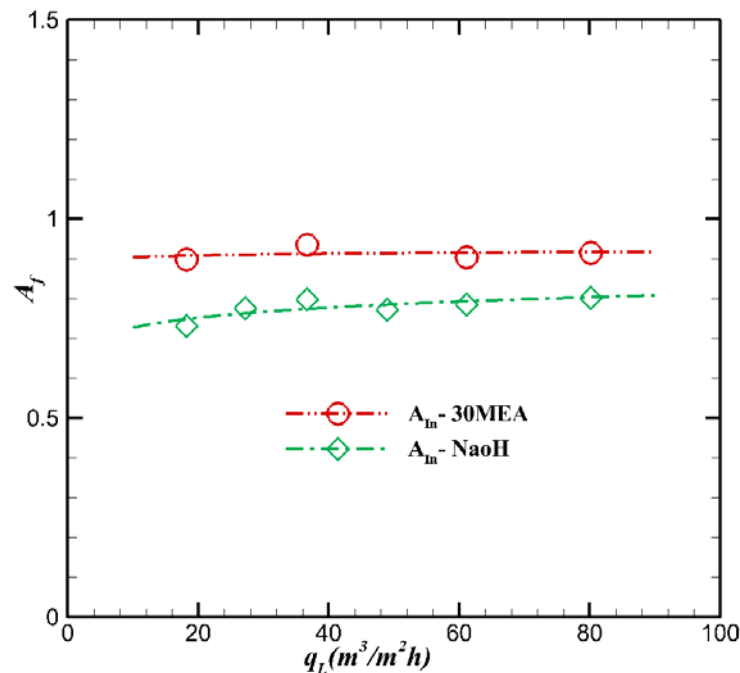


Figure 16. Effect of liquid load on the interfacial area for two solvents. 30MEA shows a slightly higher value of the interfacial area than the corresponding one for NaOH.

4.3.3 Effects of Contact Angle

The flow simulations in the REU were earlier restricted to $\gamma = 10^\circ$. Effects of contact angle were extensively studied earlier for a rivulet falling over an inclined flat plate [35] and corrugated sheet [53]. The complex nature of the variation of interfacial area with contact angle was observed for flow over an inclined plate.

40MEA was chosen as the solvent in this case. The flow simulations were conducted for a wide range of contact angles ($\gamma \sim 10\text{--}70^\circ$) at a liquid load of $62 \text{ m}^3/\text{m}^2 \text{ h}$. Consistent with previous studies [35, 53, 63, 67], the contact angle is normalized as $1 - \cos\gamma$.

The effect of contact angle on the normalized effective mass transfer (A_{eff}) and interfacial (A_{In}) areas for 40MEA at $q_L = 62 \text{ m}^3/\text{m}^2 \text{ h}$ is presented in Figure 17. Both areas are found to initially decrease with increasing γ values. However, effective area computed via chemical absorption shows higher value $\gamma > 40^\circ$, which cannot be a realistic prediction. Consequently, it fails to accurately predict the area. This discrepancy rises due to insufficient grid resolution in those cases. On the other hand, normalized interfacial area consistently decreases with increased value of contact number. The wetting characteristics of a solvent decrease with increased γ value, i.e., hydrophilic to hydrophobic nature. Consistent with previous studies [67], both interfacial areas significantly vary with contact angle. At lower γ value, the adhesive force dominates the cohesive force of the solvent, and, subsequently, enhanced wetting is observed. Further, the value of interfacial area at $\gamma = 10^\circ$ was found to be three times higher than the corresponding one for $\gamma = 70^\circ$. To illustrate this behavior, the pseudo-steady shape of the gas-liquid interface is presented in Figure 18 at $q_L = 62 \text{ m}^3/\text{m}^2 \text{ h}$ and different γ values. With decreasing contact angle ($\gamma \leq 40^\circ$), liquid exhibits enhanced spreading and transition of flow regime gradually occurs, i.e., rivulet to film flow. This behavior is consistent with the previous studies of Haroun et al. [58]. In case of rivulet flow, the solvent prefers to flow in the channel's valley in all cases. At higher γ values, liquid does not significantly spread and is constrained into the valley. As a result, thicker rivulet appears there and requires very fine mesh to accurately predict the mass transfer. A coarse mesh may predict higher mass transfer between phases. The theoretical value of the mass transfer coefficient is used in the computation of effective area, and consequently, effective mass transfer area increases. The effective area in such cases is unrealistic and can be disregarded.

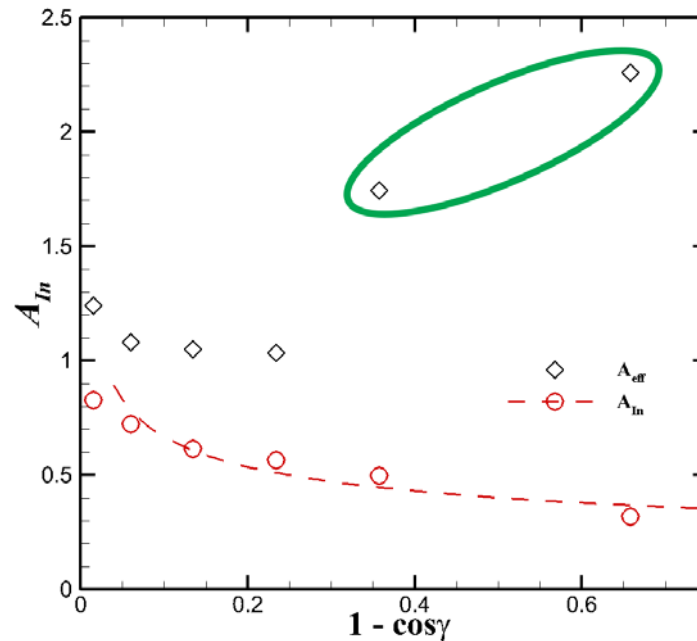


Figure 17. Variation of the normalized effective (A_{Wn}) and interfacial (A_{In}) areas with contact angle (γ) for 40MEA ($Ka=443$) at $q_L = 62 \text{ m}^3/\text{m}^2 \text{ h}$. Over prediction in the effective (points in the green elliptic boundary) at higher contact angle is a consequence of grid resolutions.

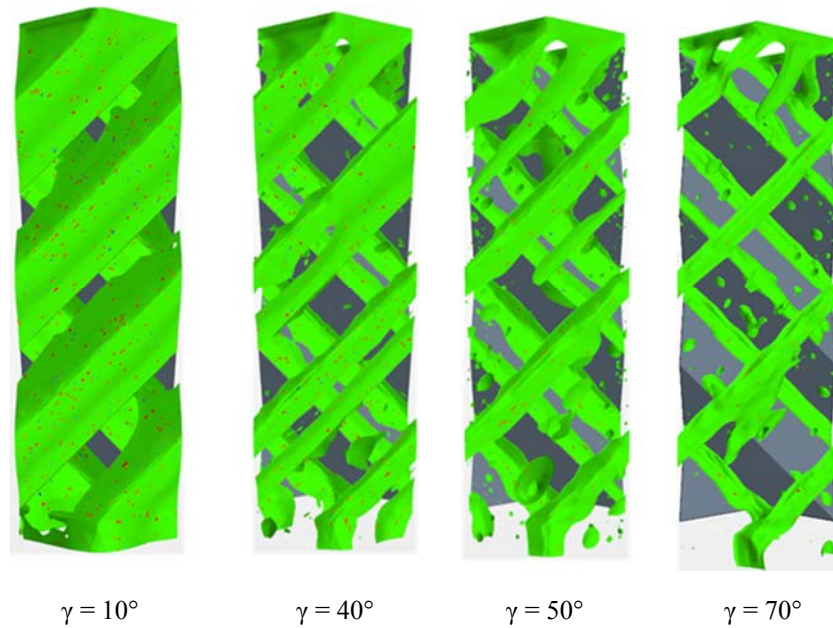


Figure 18. Pseudo-steady shape of the interface in the REU (i.e., both sheets) for 40 MEA at $q_L = 62 \text{ m}^3/\text{m}^2\text{h}$ and different contact angles ($\gamma = 70^\circ$ to $\gamma = 10^\circ$). The transition from film to rivulet flow occurs for a value around $\gamma = 40^\circ$ for this solvent.

Earlier studies by Sebastia-Saez et al. [59] could not find the film flow regime in the simulations and disregarded the presence of the film flow regime in a packed column. However, their remark is a consequence of inappropriate boundary condition (symmetry) imposed at the side of flow domain. On the contrary, other flow studies [57, 58] also found both film and rivulet flow regimes in the packings. The effect of the contact angle is found to be more pronounced in the present study than the studies by Sebastia-Saez et al. [59], who found double interfacial area when reducing γ value from 70° to 10° . Hence, their study underpredicts the effects of contact angle on the interfacial area. Similarly, Nicolaiewsky et al. [83] and Basden [57] also found a mild effect of γ on the wetted/interfacial area. Moreover, Shi and Mersmann [63] and Rocha et al. [69] found significant effect of contact angle on the interfacial area.

5.0 Multiphase Flow Simulations in Random Ring Packings

5.1 Introduction

Liquid-gas countercurrent flow in a packed tower/column plays an important role in the modern chemical industry for gas clean up applications, especially for the CO₂ capture [84]. Numerous experimental data, various correlations, and empirical formulas have been developed to describe the relationship of fluid dynamics in packed columns in different configurations [84-92]. These empirical formulas and correlations are widely used in the continuum large-scale CFD simulation to predict the CO₂ capture efficiency and other related performances. For the large-scale CFD simulation, effective reaction area or liquid-gas interface area of packing is very critical, and it is usually hard to measure in experiments. Some literature provide the empirical equations to approximate the wetted surface area of packing [22, 92]. However, because of the various packed column configurations, such as structured packing, classic random packing, modern new random packing, etc., the existing empirical equation may not be accurate enough to describe the relationship of effective reaction surface area and flow conditions. Therefore, high-resolution multiphase CFD simulation is a relatively efficient alternative to study the effective reaction surface area of packed column, which will be used in future device-scale CFD simulations.

For complicated packed column geometry, it is critical to track the liquid-gas interface in CFD models. Several multiphase CFD models have been developed for this purpose, such as the multiphase lattice Boltzmann equation (LBE) model [93, 94], the VOF method [95], and the smooth particle hydrodynamics (SPH) method [96]. VOF is the most widely used approach for capturing the dynamic liquid-gas interface, and has a higher tolerance on different fluid properties than LBE and much higher computational efficiency than SPH. Because of supporting unstructured mesh, VOF is more efficient to capture the complicated geometry, such as the random packed column.

In this section, we present an approach and framework to model the 3D multiphase flow in random packed column. The chemical absorption of CO₂ in the aqueous solution of MEA in the random packed pall ring column is used as a demonstration. The geometry and boundary conditions are introduced in the next section. The simulation results are presented in Section 5.3.

5.2 Simulation Geometry and Boundary Conditions

In this study, the pall ring geometry is shown in Figure 19(a). The diameter of the pall ring is 16 mm, the height is 16 mm, and the thickness is 0.5 mm. More detailed dimensions are marked in Figure 19(a). Pall rings fill a cylindrical container, whose diameter is 100 mm and height is 200 mm. The configuration of packed column (shown in Figure 19(b)) was generated using a discrete element method. There is a total of 160 pall rings in the packed column, and the specific area is 282 m²/m³.

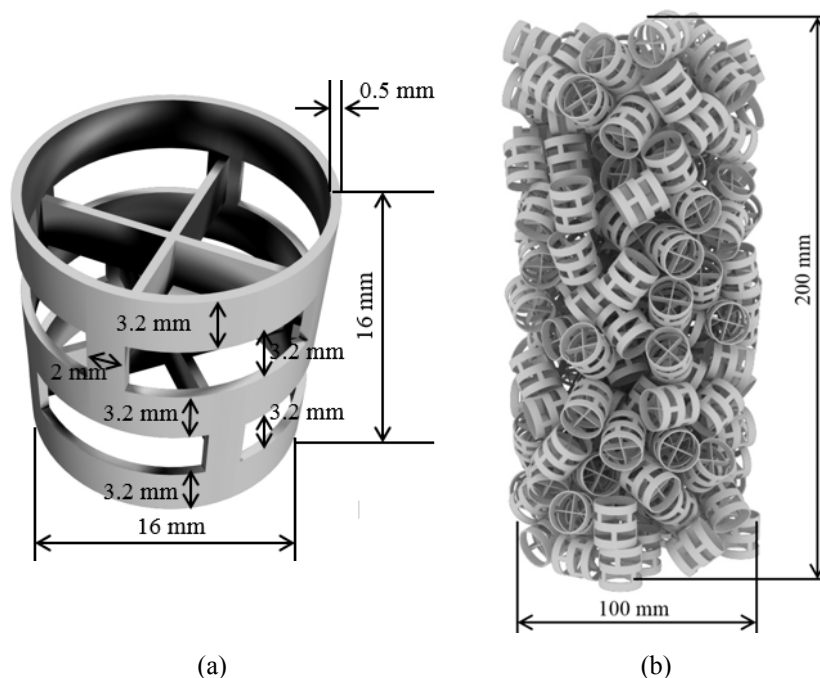


Figure 19. Geometry: (a) single pall ring dimensions; (b) random packed pall ring column.

There is a total of 13 liquid inlets on the top surface of the column, and the rest of the area on the top surface is specified as gas outlet, as shown in Figure 20(a). The red arrows represent the flow direction at gas outlet, and the blue arrows represent the flow direction at liquid inlet. The column wall is specified as the solid wall with no-slip boundary.

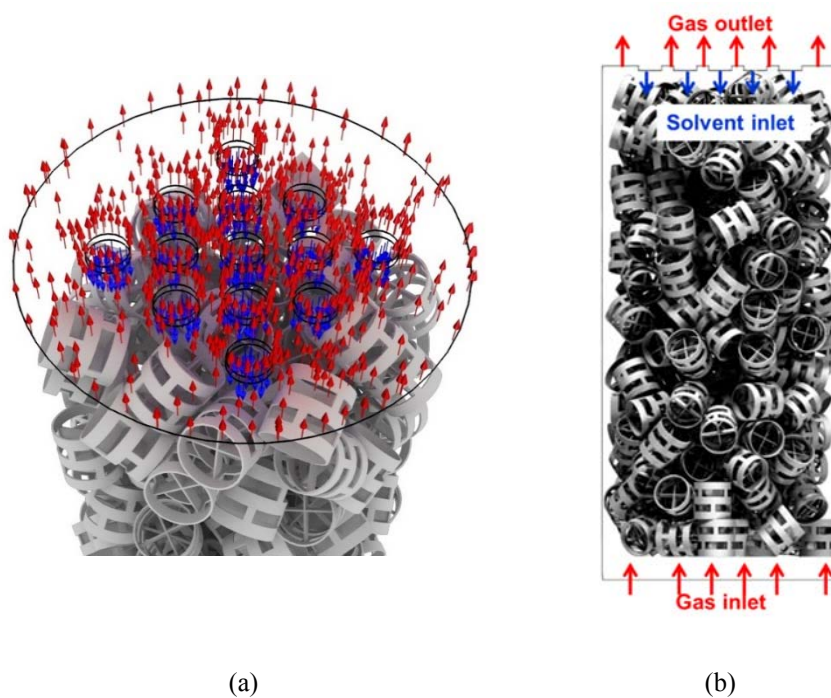


Figure 20. Inlet and outlet boundary conditions used in the flow simulations: (a) top view and (b) side view.

The bottom surface of the column is the pressure boundary for flow, and there is no gradient boundary for the volume fraction of liquid phase, as shown in Figure 20(b).

The particles packing process is modeled using a discrete element method (DEM). It is computationally too expensive to simulate the movements and interactions for the large amount of real pall rings, so each pall ring is simplified as a solid cylinder particle whose diameter and height are the same as the pall ring. For each ring, the movement is governed by

$$m_p \frac{dv_p}{dt} = F_c + F_g, \quad (55)$$

$$I_p \frac{d\omega_p}{dt} = M_c, \quad (56)$$

where m_p is the mass of the particle, v_p is the velocity of the particle, F_c is the surface contact force, F_g is gravity force, I_p is the particle moment of inertia, ω_p is particle angular velocity, and M_c is the moment acting on an individual particle due to contact force, which in turn acts on the particle at a point other than the particle center of gravity. After all the particles fill the cylindrical container and settle down, the position and orientation vector of each cylindrical particle is exported, which is used to replace the particles by real pall ring geometry.

The computational flow domain is discretized using polyhedral mesh with prism layers around the solid surface (pall ring and column wall). The prism layer is used to capture the flow field near the solid wall. There is a total of 13 M cells. The average mesh size is 0.78 mm, and mesh size standard deviation is 0.72 mm.

5.3 Results

In CFD simulation, the liquid-gas interface is defined as the iso-surface that the volume fraction of liquid (α) is 0.5, as shown by the blue lines in Figure 21. The wetted area is defined as

$$\int_{S_w} \alpha dS_w, \quad (57)$$

where S_w is the pall ring wall surface area, as shown by the red line in Figure 21.

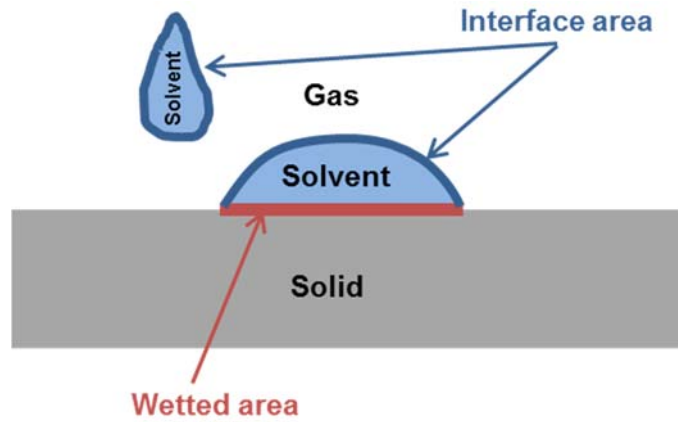


Figure 21. Sketch demonstrating the liquid-gas interface and wetted surface.

Both liquid-gas interface and wetted area are hard to measure directly in experiments. In experiments, an area is measured indirectly through chemical absorption, which is defined as the effective reaction area calculated by:

$$a_e = \frac{u_G}{k'_g Z R T} \ln \left(\frac{C_{CO_2, in}}{C_{CO_2, out}} \right), \quad (58)$$

where u_G is the gas average velocity, Z is the height of the packed column, R is the gas constant, and T is temperature. $C_{CO_2, in}$ and $C_{CO_2, out}$ are the average CO_2 concentration at packed column inlet and outlet, respectively. In this study, for eliminating the inlet and outlet boundary effects on estimation of effective reaction area, $C_{CO_2, in}$ is calculated at a cross section 80 mm above the bottom surface, and $C_{CO_2, out}$ is calculated at a cross section 180 mm above the bottom surface. Therefore, Z is the distance between the two cross sections, and is 100 mm in this study. k'_g is the mass transfer coefficient and is calculated by

$$k'_g = \frac{1}{H} \sqrt{r c_s D_L}, \quad (59)$$

Where H is Henry's constant, r is the reaction rate, c_s is the MEA concentration, and D_L is the CO_2 diffusivity in liquid. Because the reaction or absorption only occurs at the liquid-gas interface, it is assumed that the hydrodynamic liquid-gas interface area should be equivalent to the effective reaction area calculated by Eq. (58).

The concentration in MEA is 4911 mol/m^3 . The properties of the fluids are listed in Table 4. Six liquid loads are investigated, which are 12.2, 24.4, 36.7, 48.9, 61.1, and $73.3 \text{ m}^3/\text{m}^2/\text{h}$. Gas flow rate is kept at 0.28 m/sec for all liquid loads.

Table 4. Liquid and gas fluids properties.

Liquid density	$\rho_l, [kg \cdot m^{-3}]$	1058
Gas density	$\rho_g, [kg \cdot m^{-3}]$	1
Liquid viscosity	$\mu_l, [Pa \cdot s]$	0.00246
Gas viscosity	$\mu_g, [Pa \cdot s]$	1.855×10^{-5}
Surface tension coefficient	$\delta, [N \cdot m^{-1}]$	0.065
CO_2 diffusivity in liquid	$D_L, [m^2 \cdot s^{-1}]$	1×10^{-9}
CO_2 diffusivity in gas	$D_G, [m^2 \cdot s^{-1}]$	1×10^{-5}
Reaction rate	$r, [m^3 \cdot mol^{-1} \cdot s^{-1}]$	5.96
Henry's constant	$H, [-]$	1.226

Simulations were run on the PNNL Institutional Computing (PIC) high-performance computing (HPC) cluster. Each compute node has dual Intel Haswell E5-2670 CPUs giving 24 cores per node. Each simulation ran on 96 CPU cores, and around 7 hours of wall clock time of simulation can propagate 1 second of solution time.

Figure 22 shows a snapshot of volume fraction of liquid on the center cross section of the packed column for three liquid loads: 12.2, 48.9, and $73.3 \text{ m}^3/\text{m}^2/\text{h}$. Blue coloring represents liquid, grey represents gas, and white represents the cross sections of rings.

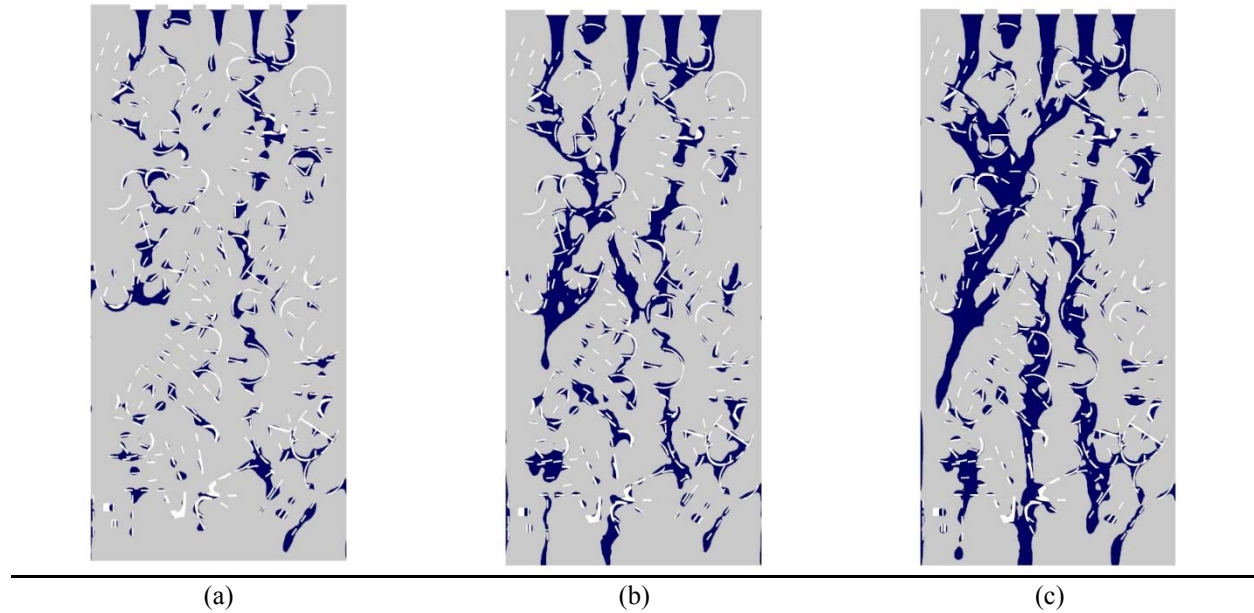


Figure 22. Liquid distribution (blue color) at the central vertical plane of the column at liquid loads (a) 12.2, (b) 48.9, and (c) 73.3 $\text{m}^3/\text{m}^2/\text{h}$.

Figure 23 shows a snapshot velocity magnitude on the center cross section of the packed column for liquid loads at 12.2, 48.9, and 73.3 $\text{m}^3/\text{m}^2/\text{h}$. Figure 24 shows a snapshot of the CO_2 concentration in the packed column for liquid loads at 12.2, 48.9, and 73.3 $\text{m}^3/\text{m}^2/\text{h}$. Figure 25 shows the CFD simulation results for the liquid-gas interface area, ring surface wetted area, and effective reaction area for comparison to the correlation (Eq. 60) developed by Song et al. [22] from regression of experimental measurements. Note that the areas presented in Figure 25 are normalized by the total area of the surface of the packed column.

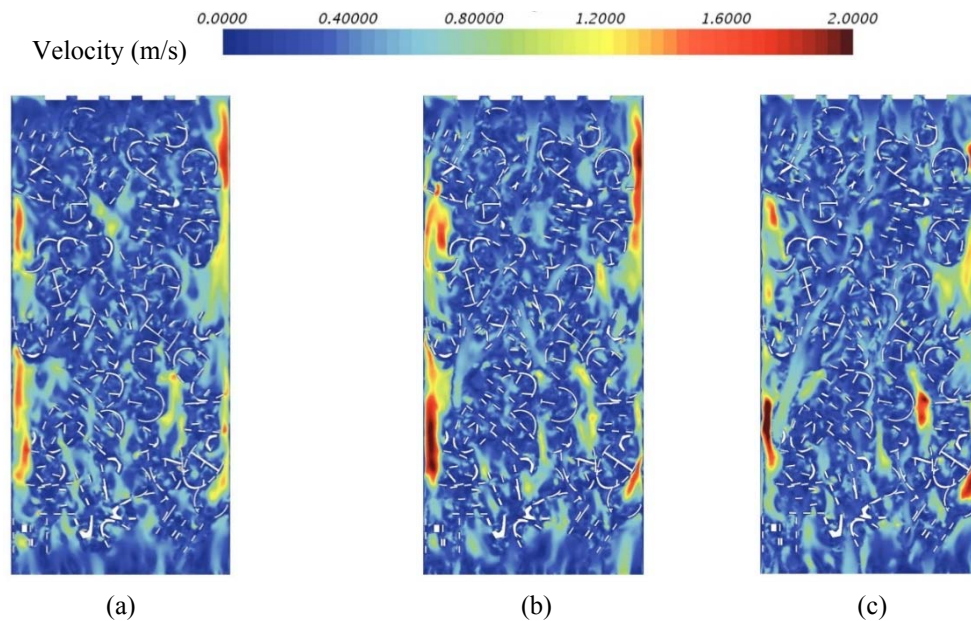


Figure 23. Velocity distribution at the central vertical plane of packed column at liquid loads: (a) 12.2, (b) 48.9, and (c) 73.3 $\text{m}^3/\text{m}^2/\text{h}$.

$$\frac{a_e}{a_p} = 1.16 \cdot \eta \cdot \left[\left(\frac{\rho_L}{\sigma} \right) \cdot g^{1/2} \cdot u_L \cdot a_p^{-3/2} \right]^{0.138}, \quad (60)$$

where a_p is the total packed geometry surface volume ratio, σ is surface tension coefficient, u_L is liquid velocity, and η is the coefficient controlled by the type and material of the packed column. For the stainless steel random ring packed column, it can be calculated by:

$$\eta = 1.34 - 0.26 \left(\frac{a_p}{250} \right). \quad (61)$$

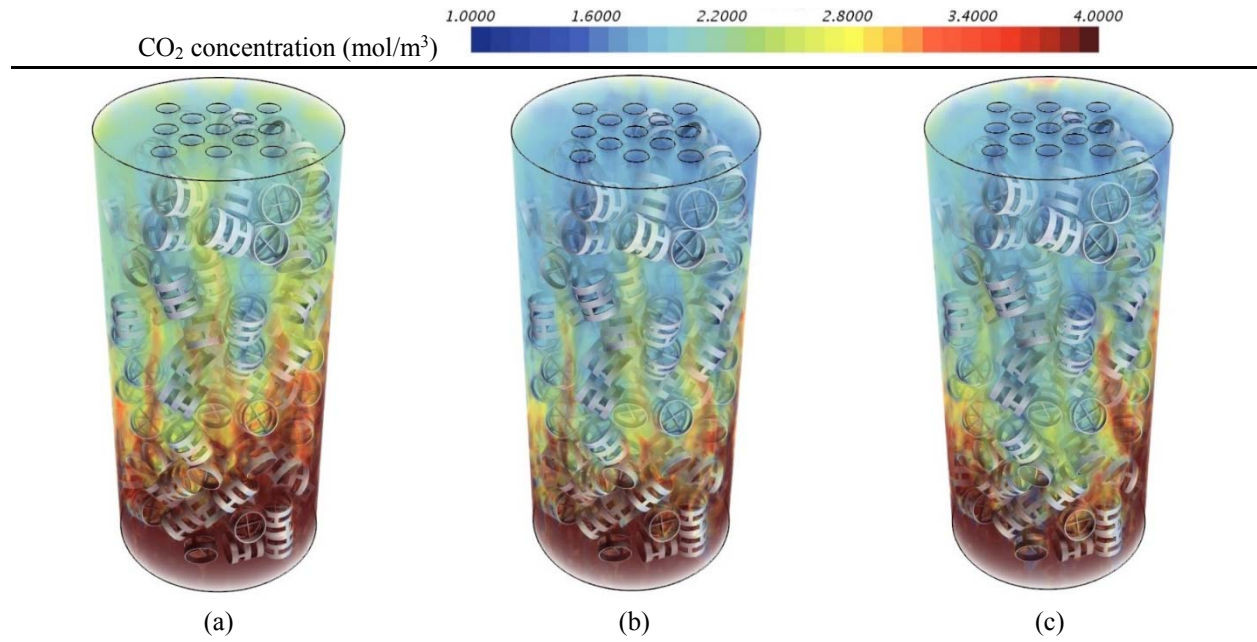


Figure 24. CO₂ concentration in the packed column at liquid loads (a) 12.2, (b) 48.9, and (c) 73.3 m³/m²/h.

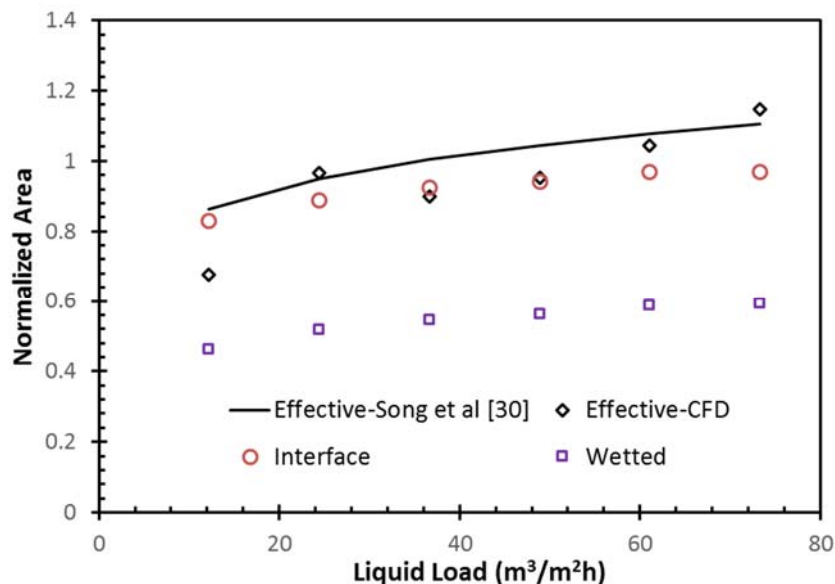


Figure 25. Comparison of the CFD-predicted effective area, gas-liquid interfacial area, wetted area, and effective area computed from the empirical correlation by Song et al. [2].

The CFD-simulated interfacial area is comparable to the effective reaction area for all liquid loads. Both areas match with the correlation equation (Eq. (60)) fairly well. The wetted area is calculated according to Eq. (57), which is much smaller than the liquid-gas interface area and effective reaction area. Unlike the structured packed columns, the complicated cluster of rings forms a discontinuous structure in the random ring packed column. Therefore, when liquid flows from the top to bottom of the column, it is forced to flow into the open space between ring surfaces, and forms rivulet or stream flow in the void space, as shown in Figure 26. The blue part is the liquid, the grey part is the gas, and the white part is the solid ring. The orange line marks an example of the liquid-gas interface, and the red line marks an example of the wetted ring surface. In the zoomed view of the cross section of the random ring packed column, as shown in Figure 26, the liquid-gas interface is much larger than the wetted ring surface.

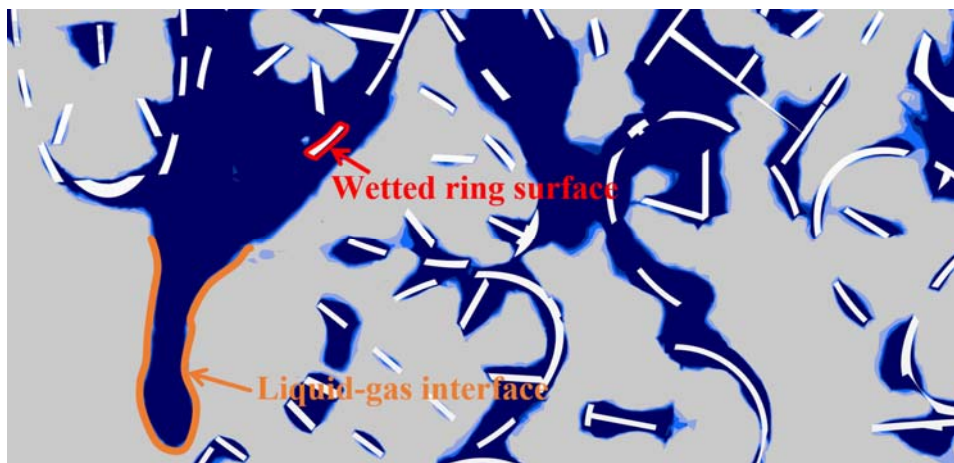


Figure 26. Zoomed view of a cross section of the random ring packed column. The blue and grey color denote the liquid and gas phase, respectively.

6.0 Conclusion

Post-combustion carbon capture via solvent absorption has gained significant interest among researchers because of its prospective deployment in the mitigation of greenhouse gas emission. The solvent absorption is carried out through countercurrent gas-liquid flow in a structured packed column. The CFD modeling of such a system is a complex problem because of the wide disparity in the length scales; therefore, a multiscale modeling approach is needed. The local hydrodynamic (microscale) plays a key role in the overall efficiency.

The mass transfer between the gas and liquid phases plays a critical role in determining the column height. Recent experiments have found that the direct impact of viscosity on mass transfer is larger for a packed column ($k_L \sim \mu^{-0.40}$) compared to WWC ($k_L \sim \mu^{-0.17}$). In principle, this direct influence of viscosity on the mass transfer coefficient may be due to the liquid turbulence enhanced mass transfer in a packed column. In this context, detailed analytical studies and numerical simulations have been conducted to explain the underlying physics behind such discrepancy. Wavy film flow is proposed as a major mechanism responsible for the discrepancy and expressions for eddy-enhanced diffusivity, and the mass transfer coefficient for wavy film falling over a flat plate is derived based on the fundamental hydrodynamic and mass transfer equations. It demonstrates a much higher dependence of mass transfer on viscosity and solvent flow rate in accordance with the experiment. In addition, to investigate the direct impact of viscosity on the mass transfer coefficient, multiphase flow simulation has been conducted for WWCs and ZZCs. ZZC was chosen for its 2D representation of a structured packed column. The predicted value of average film thickness (δ_{av}) matches well with Nusselt theory. The value of δ_{av} increases with increased value of solvent viscosity. For a periodic wavy film, the normalized wavelength increases with increased Kapitza number, i.e., decreased viscosity. The WWC and ZZC show almost identical wavelength values, except at low viscosity where the WWC shows a slightly higher value. Notably, the mass transfer coefficient for a wavy film shows larger dependence on the viscosity compared to a flat uniform film, which is true for both WWC and ZZC. This dependence from simulations generally agrees with the observation ($k_L \sim v_L^{-0.35 \sim -0.4}$) found in both theoretical and experimental studies.

Apart from mass transfer coefficient, interfacial/effective area is another critical parameter dictating the overall mass transfer between phases. In the solvent absorption system due to reaction kinetics, mass transfer due to physical absorption is negligible compared to the corresponding one, which is due to reactive mass transfer. In the reactive mass transfer, higher interfacial area is desirable. Accordingly, 3D reactive multiphase flow simulations using the VOF method were conducted to investigate microscale hydrodynamics in the REU of a packed column. Particularly, the impact of solvent properties, solid surface characteristics, and liquid loads on the interfacial area were extensively investigated. The effective area is computed by the indirect method suggested by Danckwerts and direct measurements of the the gas-liquid interface. In principle, the effective area measured by Danckwerts methods should be the same as interfacial area. The CFD-predicted effective area matches well with the corresponding experimental value. On the other hand, the interfacial area shows a lower value of the mass transfer area. The lower value of the interfacial area might be due to the higher prediction of mass transfer across the interface. Apart from 0.1 M NaOH aqueous solvent, the CFD-predicted effective area was also compared with 0.30x and 0.40x MEA aqueous solvents. The effect of the contact angle was also extensively investigated, and the interfacial area increases with decreasing contact angle at a fixed flow rate for a given solvent. Similar to previous studies [53], the transition of the flow regimes was observed with changes in the value of contact angle. It exhibits an inverse relationship, i.e., film flow to rivulet flow with increasing contact angle ($\gamma > 40^\circ$).

In the subsequent studies, a similar approach is introduced to investigate the reactive mass transfer in a lab-scale random ring packed column. The simulation results demonstrate that the proposed approach is computationally affordable. The CFD-simulated liquid-gas interfacial area is similar to the effective reaction area, and they are both comparable to the empirical correlation. Eventually, the proposed procedure can be extended to other types of random packed columns and different solvents. Additionally, both the liquid-gas interface and effective reaction area are larger than the wetted ring surface area. The complicated ring surface is discontinuous in the random packed column, and the liquid is forced to flow into the void space between ring surfaces, which is not observed in the structure packing column.

7.0 References

1. Hirt, C.W. and B.D. Nichols, *Volume of fluid (VOF) method for the dynamics of free boundaries*. Journal of Computational Physics, 1981. **39**(1): p. 201-225.
2. Brackbill, J.U., D.B. Kothe, and C. Zemach, *A continuum method for modeling surface tension*. Journal of Computational Physics, 1992. **100**(2): p. 335-354.
3. Haroun, Y., D. Legendre, and L. Raynal, *Direct numerical simulation of reactive absorption in gas-liquid flow on structured packing using interface capturing method*. Chemical Engineering Science, 2010. **65**(1): p. 351-356.
4. Haroun, Y., D. Legendre, and L. Raynal, *Volume of fluid method for interfacial reactive mass transfer: Application to stable liquid film*. Chemical Engineering Science, 2010. **65**(10): p. 2896-2909.
5. Marschall, H., et al., *Numerical simulation of species transfer across fluid interfaces in free-surface flows using OpenFOAM*. Chemical Engineering Science, 2012. **78**: p. 111-127.
6. Wang, C., et al., *Hierarchical calibration and validation framework of bench-scale computational fluid dynamics simulations for solvent-based carbon capture. Part 2: Chemical absorption across a wetted wall column*. Greenhouse Gases: Science and Technology, 2018. **8**(1): p. 150-160.
7. Danckwerts, P.V., *The reaction of CO₂ with ethanolamines*. Chemical Engineering Science, 1979. **34**(4): p. 443-446.
8. Pohorecki, R. and W.d.w. Moniuk, *Kinetics of reaction between carbon dioxide and hydroxyl ions in aqueous electrolyte solutions*. Chemical Engineering Science, 1988. **43**(7): p. 1677-1684.
9. Haroun, Y., L. Raynal, and D. Legendre, *Mass transfer and liquid hold-up determination in structured packing by CFD*. Chemical Engineering Science, 2012. **75**: p. 342-348.
10. Jou, F.-Y., A.E. Mather, and F.D. Otto, *The solubility of CO₂ in a 30 mass percent monoethanolamine solution*. The Canadian Journal of Chemical Engineering, 1995. **73**(1): p. 140-147.
11. Caplow, M., *Kinetics of carbamate formation and breakdown*. Journal of the American Chemical Society, 1968. **90**(24): p. 6795-6803.
12. Aboudheir, A., et al., *Kinetics of the reactive absorption of carbon dioxide in high CO₂-loaded, concentrated aqueous monoethanolamine solutions*. Chemical Engineering Science, 2003. **58**(23-24): p. 5195-5210.
13. Hikita, H., et al., *The kinetics of reactions of carbon dioxide with monoethanolamine, diethanolamine and triethanolamine by a rapid mixing method*. The Chemical Engineering Journal, 1977. **13**(1): p. 7-12.
14. *ANSYS Fluent Theory Guide*. 2015.
15. Muzafarrija, S. and M. Perić, *Computation of free surface flows using the finite volume method and moving grids*. Numerical Heat Transfer, Part B: Fundamentals, 1997. **32**(4): p. 369-384.
16. Patankar, S.V., *Numerical heat transfer and fluid flow*. 1980, Washington; New York: Hemisphere Pub. Corp. ; McGraw-Hill.
17. Whitman, W.G., *The two film theory of gas absorption*. International Journal of Heat and Mass Transfer, 1962. **5**(5): p. 429-433.
18. Higbie, R., *The rate of absorption of a pure gas into a still liquid during short periods of exposure*. Transactions of the American Institute of Chemical Engineers, 1935. **31**: p. 365-389.
19. Danckwerts, P.V., *Significance of Liquid-Film Coefficients in Gas Absorption*. Industrial & Engineering Chemistry, 1951. **43**(6): p. 1460-1467.
20. Biń, A.K., *Mass transfer into a turbulent liquid film*. International Journal of Heat and Mass Transfer, 1983. **26**(7): p. 981-991.
21. Song, D., A.F. Seibert, and G.T. Rochelle, *Effect of Liquid Viscosity on the Liquid Phase Mass Transfer Coefficient of Packing*. Energy Procedia, 2014. **63**: p. 1268-1286.

22. Song, D., A.F. Seibert, and G.T. Rochelle, *Mass Transfer Parameters for Packings: Effect of Viscosity*. Industrial & Engineering Chemistry Research, 2018. **57**(2): p. 718-729.
23. Tsai, R.E., et al., *Influence of viscosity and surface tension on the effective mass transfer area of structured packing*. Energy Procedia, 2009. **1**(1): p. 1197-1204.
24. Tsai, R.E., et al., *A dimensionless model for predicting the mass-transfer area of structured packing*. AIChE Journal, 2011. **57**(5): p. 1173-1184.
25. Wang, C., et al., *Packing Characterization for Post Combustion CO₂ Capture: Mass Transfer Model Development*. Energy Procedia, 2014. **63**: p. 1727-1744.
26. Ataki, A. and H.J. Bart, *Experimental and CFD simulation study for the wetting of a structured packing element with liquids*. Chemical Engineering & Technology, 2006. **29**(3): p. 336-347.
27. Fernandes, J., et al., *Application of CFD in the study of supercritical fluid extraction with structured packing: Wet pressure drop calculations*. The Journal of Supercritical Fluids, 2009. **50**(1): p. 61-68.
28. Hosseini, S.H., et al., *Computational fluid dynamics studies of dry and wet pressure drops in structured packings*. Journal of Industrial and Engineering Chemistry, 2012. **18**(4): p. 1465-1473.
29. Raynal, L., C. Boyer, and J.-P. Ballaguet, *Liquid Holdup and Pressure Drop Determination in Structured Packing with CFD Simulations*. The Canadian Journal of Chemical Engineering, 2004. **82**(5): p. 871-879.
30. Petre, C.F., et al., *Pressure drop through structured packings: Breakdown into the contributing mechanisms by CFD modeling*. Chemical Engineering Science, 2003. **58**(1): p. 163-177.
31. Nieves-Remacha, M.J., L. Yang, and K.F. Jensen, *OpenFOAM Computational Fluid Dynamic Simulations of Two-Phase Flow and Mass Transfer in an Advanced-Flow Reactor*. Industrial & Engineering Chemistry Research, 2015. **54**(26): p. 6649-6659.
32. Wang, C., et al., *Beyond the standard two-film theory: Computational fluid dynamics simulations for carbon dioxide capture in a wetted wall column*. Chemical Engineering Science, 2018. **184**: p. 103-110.
33. Wang, C., et al., *Hierarchical calibration and validation for modeling bench-scale solvent-based carbon capture. Part I: Non-reactive physical mass transfer across the wetted wall column*. Greenhouse Gases: Science and Technology, 2017. **7**(4): p. 706-720.
34. Hu, J., et al., *Numerical simulation of carbon dioxide (CO₂) absorption and interfacial mass transfer across vertically wavy falling film*. Chemical Engineering Science, 2014. **116**: p. 243-253.
35. Singh, R.K., J.E. Galvin, and X. Sun, *Three-dimensional simulation of rivulet and film flows over an inclined plate: Effects of solvent properties and contact angle*. Chemical Engineering Science, 2016. **142**: p. 244-257.
36. Singh, R.K., et al., *Breakup of a liquid rivulet falling over an inclined plate: Identification of a critical Weber number*. Physics of Fluids, 2017. **29**(5): p. 052101.
37. Sebastia-Saez, D., et al., *3D modeling of hydrodynamics and physical mass transfer characteristics of liquid film flows in structured packing elements*. International Journal of Greenhouse Gas Control, 2013. **19**(0): p. 492-502.
38. Pigford, R.L., *Counter-Diffusion in a Wetted Wall Column*, in *Department of Chemistry and Chemical Engineering*. 1941, University of Illinois.
39. Pacheco, M.A., *Mass Transfer, Kinetics and Rate-Based Modeling of Reactive Absorption*, in *Chemical Engineering*. 1998, The University of Texas at Austin: Austin, TX.
40. Patnaik, V. and H. PerezBlanco, *Roll waves in falling films: An approximate treatment of the velocity field*. International Journal of Heat and Fluid Flow, 1996. **17**(1): p. 63-70.
41. Nusselt, W., *Die Oberflächenkondensation des Wasserdampfes*. Zeitschrift des Vereines Deutscher Ingenieure 1916. **60**(27): p. 541-546.
42. Yih, S.M., *Modeling heat and mass transfer in wavy and turbulent falling liquid films*. Wärme - und Stoffübertragung, 1987. **21**(6): p. 373-381.
43. Odier, P., et al., *Fluid mixing in stratified gravity currents: the Prandtl mixing length*. Phys Rev Lett, 2009. **102**(13): p. 134504.

44. Shkadov, V.Y., *Wave flow regimes of a thin layer of viscous fluid subject to gravity*. Fluid Dynamics, 1967. **2**(1): p. 29-34.
45. CD-adapco *STAR-CCM+ 10.04 User Guide*. 2015.
46. Gu, F., et al., *CFD Simulation of Liquid Film Flow on Inclined Plates*. Chemical Engineering & Technology, 2004. **27**(10): p. 1099-1104.
47. Lockett, M.J. and J.F. Billingham, *The Effect of Maldistribution on Separation in Packed Distillation Columns*. Chemical Engineering Research and Design, 2003. **81**(1): p. 131-135.
48. Raynal, L. and A. Royon-Lebeaud, *A multi-scale approach for CFD calculations of gas-liquid flow within large size column equipped with structured packing*. Chemical Engineering Science, 2007. **62**(24): p. 7196-7204.
49. Owens, S.A., et al., *Computational Fluid Dynamics Simulation of Structured Packing*. Industrial & Engineering Chemistry Research, 2013. **52**(5): p. 2032-2045.
50. Iso, Y., et al., *Numerical and Experimental Study on Liquid Film Flows on Packing Elements in Absorbers for Post-combustion CO₂ Capture*. Energy Procedia, 2013. **37**(0): p. 860-868.
51. Olujic, Z., *Development of a complete simulation model for predicting the hydraulic and separation performance or distillation columns equipped with structured packings*. Chemical and Biochemical Engineering Quarterly, 1997. **11**(1): p. 31-46.
52. Li, H., et al., *Liquid flow behavior study in SiC foam corrugated sheet using a novel ultraviolet fluorescence technique coupled with CFD simulation*. Chemical Engineering Science, 2015. **123**: p. 341-349.
53. Singh, R.K., J.E. Galvin, and X. Sun, *Hydrodynamics of the rivulet flow over corrugated sheet used in structured packings*. International Journal of Greenhouse Gas Control, 2017. **64**: p. 87-98.
54. Subramanian, K., et al., *Analysis of Hydrodynamics of Fluid Flow on Corrugated Sheets of Packing*. International Journal of Chemical Engineering, 2012. **2012**: p. 13.
55. Bradtmöller, C., et al., *Influence of Viscosity on Liquid Flow Inside Structured Packings*. Industrial & Engineering Chemistry Research, 2015. **54**(10): p. 2803-2815.
56. Shojaee, S., et al., *Prediction of the Effective Area in Structured Packings by Computational Fluid Dynamics*. Industrial & Engineering Chemistry Research, 2011. **50**(18): p. 10833-10842.
57. Basden, M.A., *Characterization of Structured Packing via Computational Fluid Dynamics*, in *Chemical Engineering*. 2014, The University of Texas at Austin: Austin. p. 306.
58. Haroun, Y., L. Raynal, and P. Alix, *Prediction of effective area and liquid hold-up in structured packings by CFD*. Chemical Engineering Research and Design, 2014. **92**(11): p. 2247-2254.
59. Sebastia-Saez, D., et al., *Meso-scale CFD study of the pressure drop, liquid hold-up, interfacial area and mass transfer in structured packing materials*. International Journal of Greenhouse Gas Control, 2015. **42**: p. 388-399.
60. Rizzuti, L. and A. Brucato, *Liquid viscosity and flow rate effects on interfacial area in packed columns*. The Chemical Engineering Journal, 1989. **41**(1): p. 49-52.
61. Fourati, M., V. Roig, and L. Raynal, *Experimental study of liquid spreading in structured packings*. Chemical Engineering Science, 2012. **80**: p. 1-15.
62. Snoeijer, J.H. and B. Andreotti, *A microscopic view on contact angle selection*. Physics of Fluids, 2008. **20**(5): p. 057101.
63. Shi, M.G. and A. Mersmann, *Effective interfacial area in packed columns*. German chemical engineering, 1985. **8**(2): p. 87-96.
64. Kohrt, M., et al., *Texture influence on liquid-side mass transfer*. Chemical Engineering Research and Design, 2011. **89**(8): p. 1405-1413.
65. Wenzel, R.N., *Resistance of solid surfaces to wetting by water*. Industrial & Engineering Chemistry, 1936. **28**(8): p. 988-994.
66. Nicolaiewsky, E.M.A. and J.R. Fair, *Liquid Flow over Textured Surfaces. I. Contact Angles*. Industrial & Engineering Chemistry Research, 1998. **38**(1): p. 284-291.
67. Singh, R.K., J.E. Galvin, and X. Sun, *Multiphase flow studies for microscale hydrodynamics in the structured packed column*. Chemical Engineering Journal, 2018. **353**: p. 949-963.

68. Billet, R. and M. Schultes, *Prediction of Mass Transfer Columns with Dumped and Arranged Packings*. Chemical Engineering Research and Design, 1999. **77**(6): p. 498-504.
69. Rocha, J.A., J.L. Bravo, and J.R. Fair, *Distillation columns containing structured packings: a comprehensive model for their performance. 1. Hydraulic models*. Industrial & Engineering Chemistry Research, 1993. **32**(4): p. 641-651.
70. Gualito, J.J., et al., *Design Method for Distillation Columns Filled with Metallic, Ceramic, or Plastic Structured Packings*. Industrial & Engineering Chemistry Research, 1997. **36**(5): p. 1747-1757.
71. Brunazzi, E., et al., *Interfacial area of mellapak packing: Absorption of 1,1,1-trichloroethane by Genosorb 300*. Chemical Engineering & Technology, 1995. **18**(4): p. 248-255.
72. de Brito, M.H., et al., *Effective Mass-Transfer Area in a Pilot Plant Column Equipped with Structured Packings and with Ceramic Rings*. Industrial & Engineering Chemistry Research, 1994. **33**(3): p. 647-656.
73. Olujić, Ž., A.B. Kamerbeek, and J. de Graauw, *A corrugation geometry based model for efficiency of structured distillation packing*. Chemical Engineering and Processing: Process Intensification, 1999. **38**(4): p. 683-695.
74. Olujić, Ž., A.F. Seibert, and J.R. Fair, *Influence of corrugation geometry on the performance of structured packings: an experimental study*. Chemical Engineering and Processing: Process Intensification, 2000. **39**(4): p. 335-342.
75. Siminiceanu, I., et al., *Measuring the Effective Mass Transfer Area of a Structured Packing by a Chemical Method*. Revista De Chimie, 2008. **59**(10): p. 1117-1121.
76. Green, C.W., et al., *Novel Application of X-ray Computed Tomography: Determination of Gas/Liquid Contact Area and Liquid Holdup in Structured Packing*. Industrial & Engineering Chemistry Research, 2007. **46**(17): p. 5734-5753.
77. Yang, L., *CFD Modeling of Multiphase Counter-Current Flow in Packed Bed Reactor for Carbon Capture*, in *Mechanical Engineering 2015*, University of Kentucky: Lexington, Kentucky. p. 120.
78. Tsai, R.E., et al., *Influence of Surface Tension on Effective Packing Area*. Industrial & Engineering Chemistry Research, 2008. **47**(4): p. 1253-1260.
79. Rocha, J.A., J.L. Bravo, and J.R. Fair, *Distillation columns containing structured packings: A comprehensive model for their performance. 2. Mass-transfer model*. Industrial & Engineering Chemistry Research, 1996. **35**(5): p. 1660-1667.
80. Tsai, R.E., *Mass Transfer Area of Structured Packing*, in *Chemical Engineering*. 2010, The University of Texas at Austin: Austin, TX. p. 400.
81. Singh, R.K., et al. *Numerical Simulation for Interfacial Forces of Counter-Current Flow over an Inclined Plate*. in *12th International Conference on Gas-Liquid & Gas-Liquid-Solid Reactor Engineering (GLS12)*. 2015. AIChE.
82. Bravo, J.L. and J.R. Fair, *Generalized correlation for mass transfer in packed distillation columns*. Industrial & Engineering Chemistry Process Design and Development, 1982. **21**(1): p. 162-170.
83. Nicolaiewsky, E.M.A., et al., *Liquid film flow and area generation in structured packed columns*. Powder Technology, 1999. **104**(1): p. 84-94.
84. Chen, Z., et al., *The effect of fly ash on fluid dynamics of CO₂ scrubber in coal-fired power plant*. Chemical Engineering Research and Design, 2012. **90**: p. 328-335.
85. Spedding, P.L., *Ammonia absorption into water in a packed tower I. characterization of packing and liquid distribution*. Chem. Eng. J., 1986. **32**: p. 65-76.
86. Kouri, R.J. and J. Sohlo, *Liquid and gas flow patterns in random packings*. Chem. Eng. J., 1996. **61**: p. 95-105.
87. Heymes, F., et al., *Hydrodynamics and mass transfer in a packed column: case of toluene absorption with a viscous absorbent*. Chem. Eng. Sci., 2006. **61**: p. 5094-5106.
88. Alix, P. and L. Raynal, *Liquid distribution and liquid hold-up in modern high capacity packings*. Chem. Eng. Res. Des., 2008. **86**: p. 585-591.

89. Piche, S., F. Larachi, and B.P. Grandjean, *Improved liquid hold-up correlation for randomly packed towers*. Trans. Icheme, 2001a. **79**
90. Piche, S., F. Larachi, and B.P. Grandjean, *Loading capacity in packed tower-database, correlations and analysis*. Chem. Eng. technol., 2001b. **24**(4): p. 373-380.
91. Piche, S., F. Larachi, and B.P. Grandjean, *Improving the prediction of irrigated pressure drop in packed absorption towers*. J. Chem. Eng. , 2001c. **79**.
92. Onda, K., H. Takeuchi, and Y. Okumoto, *Mass transfer coefficients between gas and liquid phases in packed columns*. Journal of Chemical Engineering of Japan, 1968. **1**(1): p. 56-62.
93. Shan, X. and H. Chen, *Lattice Boltzmann model for simulating flows with multiple phases and components*. Phys. Rev. E, 1993. **47**(3): p. 1815-1819.
94. Yuan, P. and L. Schaefer, *Equations of state in a lattice Boltzmann model*. Physics of Fluids, 2006. **18**(4).
95. Yazdi, J., et al., *3D simulation of flow around a single spur dike with free-surface flow*. International Journal of River Basin Management, 2010. **8**(1): p. 55-62.
96. Kazemi, E., et al., *Potential application of mesh-free SPH method in turbulent river flow*, in *Hydrodynamic and Mass Transport at Freshwater Aquatic Interfaces*, P.M. Rowinski and A. Marion, Editors. 2016, Springer: Switzerland.